AN ABSTRACT OF THE THESIS OF

Juergen Anders for the degree of Master of Science in Physics presented on August 1, 1988.

Title: Evolution of Optical Polarization in Single Mode Fibers

Abstract approved: Redacted for Privacy

Clifford Fairchild

This study investigates the polarization and magnetooptic properties of single-mode fibers. These are important for the development of single-mode fiber applications such as interferometric and electromagnetic field sensors and coherent communication systems, which rely on the polarization state of the light. Various linear, circular and induced birefringence effects cause mode coupling and change the state of polarization along the fiber. An additional rotation of polarized light is introduced by the geometry of the fiber. A theoretical treatment is given for these effects, serving as a basis to describe the evolution of polarization in single mode fibers.

The recently developed theory of Berry's phase as a topological effect in momentum space causing a rotation of polarized light is verified experimentally and included in the general theory of optical systems. Measurements of fiber specifications such as the elastooptic coefficient and the intrinsic birefringence are performed for two different types of fibers. The results are finally used to investigate the applicability of the geometric rotation in magnetooptic current sensing.

Evolution of Polarization along a Single Mode Fiber

by

Juergen Anders

A THESIS

submitted to

Oregon State University

in partial fulfillment of
the requirements for the
degree of

Master of Science

Completed August 1, 1988

Commencement June 1989

APPROVED:

Redacted for Privacy

Professor of Physics, in charge of major

Redacted for Privacy

Head of department, Physics

Redacted for Privacy

Dean of Graduate School

Date thesis is presented August 1, 1988

Typed by Juergen Anders for Juergen Anders

Table of Contents

List of Figures

List of Tables

Evolution of Optical Polarization in Single Mode Fibers

1. Introduction

1.1 Optical Fibers

Since its invention about 20 years ago, the silica glass fiber has become an important long distance waveguide which is used mainly as an optical communication transmission medium. This success is due to the reduction of optical losses by elimination of absorbing impurities and improvements in the material composition. The development of fiber-drawing techniques allowed better control over the forming process, which gave rise to a whole variety of different fiber designs. Besides long distance transmission lines for optical communications, new fields of applications have been opened to fiber optics technology. Particularly, the development of single-mode and polarization-maintaining fibers has been a great advance, giving the possibility of building fiber optic devices which rely on the polariztion state of the light. Polarimetric sensors for electromagnetic fields, pressure, strain and temperature have been realized, and the powerful technique of interferometric sensing has allowed construction of highly sensitive devices such as fiber-optic gyroscopes. The major advance, however, is that the use of single-mode fibers has improved optical communication due to the reduction of signal distortion and mode coupling.

In general an optical fiber consists of a central light-carrying core, surrounded by a cylindrical region called the cladding. The cladding then is covered with a protective plastic jacket, called the

buffer coating. Due to the difference in the index of refraction between core and cladding, the light is guided inside the core. In the ray picture, the concept of total internal reflection makes the interface look like a perfect mirror. The cladding, having an index of refraction smaller than the core, provides a definite fractional refractive index difference everywhere along the fiber of [1]

$$\Delta = \frac{(n_{co}-n_{cl})}{n_{co}} \qquad (1.1.1).$$

This makes the guiding properties insensitive to external contact media. In order to limit the number of modes carried by the fiber, there is only a small difference in the index of refraction and the critical angle for total internal reflection using Snell's law [4]

$$\sin(\theta_{crit}) = \frac{n_{cl}}{n_{co}} \qquad (1.1.2)$$

is very large. The numerical aperture, NA, is the measure of the maximum angle of the incident light collected by an optical system. For an optical fiber this is given by [1]

$$NA = (n_{co}^2-n_{cl}^2)^{\frac{1}{2}} = n_0 \cdot \sin\theta_{max} \qquad (1.1.3)$$

where n_0 is the index of refraction of air and θ_{max} is the maximum angle of incidence. Due to the large critical angle the NA is small, requiring the light incident from air into the end of the fiber to be nearly parallel to the fiber axis. Fibers with a small fractional refractive index, $\Delta \ll 1$, are classified as weakly guiding waveguides.[3]

The two main groups of fibers are the step-index and the graded-index fibers, which differ in the refractive index profile of core and cladding. The radial variation in the refractive index is achieved by appropriately doping the core with higher index germania and the cladding with fluorosilicates. Fig. 1.1.a shows the basic fiber geometries and guided waves in the ray picture.[1,4]

The ray picture, however, is only an approximation which is valid when the system dimensions are much bigger than the wavelength of the light. In an optical fiber a better description is given by the waveguide theory, which is introduced in chapter 1.2.

The overall properties of a fiber are determined mainly by the shape and dimension of the core. Typical core diameters in fibers used for communications range from 4-8μm for single mode fibers to 50-100μm for multimode fibers. Even larger core fibers, having diameters in the range 200-1000μm, are used in power transmission applications. For multimode fibers the cladding diameter will be between 125-140μm whereas single mode fibers are as small as 80μm. The core diameter determines the number of modes carried by the fiber and the power transmission capability. In order to gain control of the polarization in single mode fibers, the shape of the core has been modified in various ways to produce various kinds of polarization-maintaining fibers. Fig.1.1.b shows this variety.[30]

In the present study the research has been done with round core low birefringence single mode fiber.

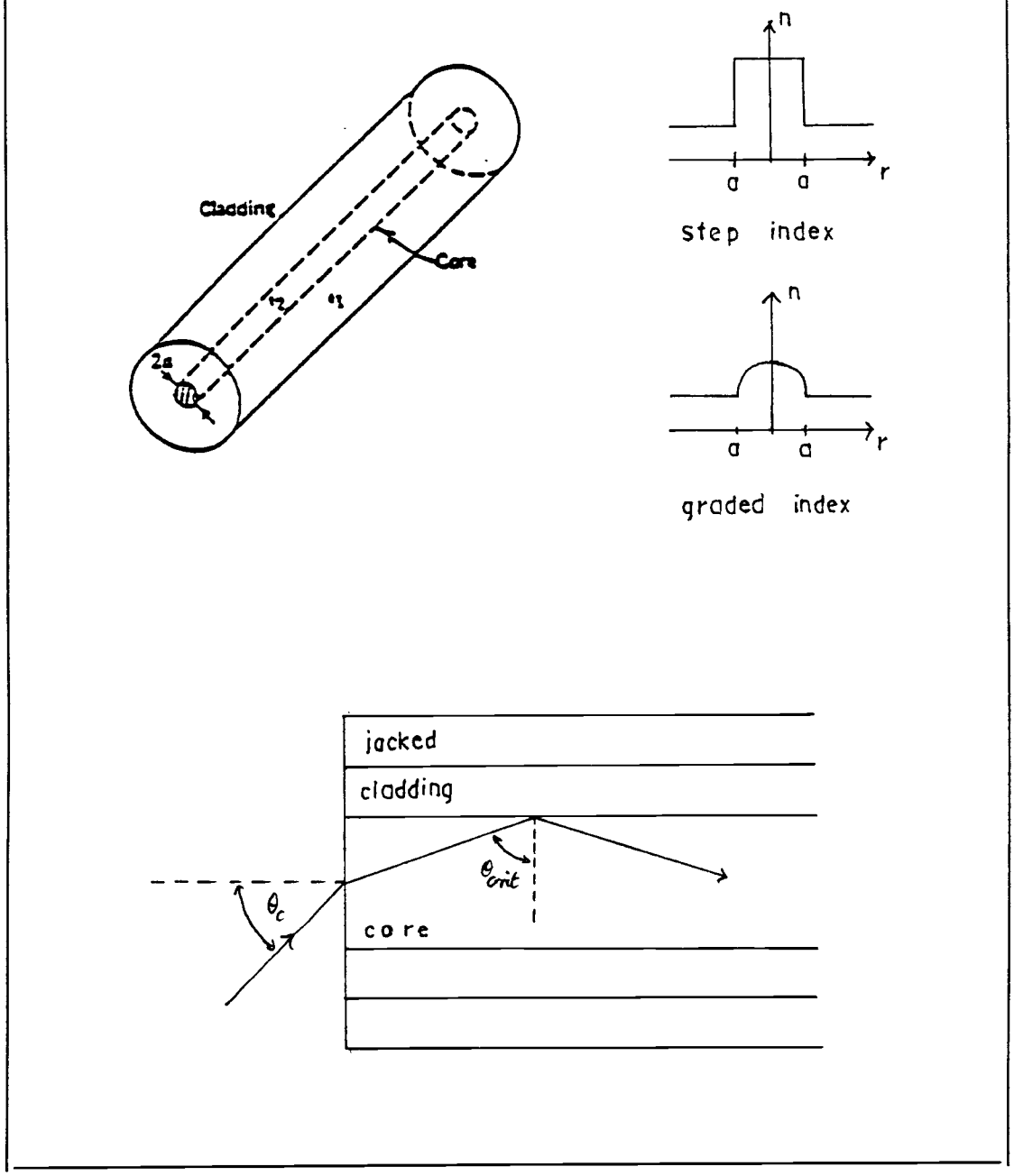

Fig. 1.1.a Fiber geometry, index profiles and the ray picture

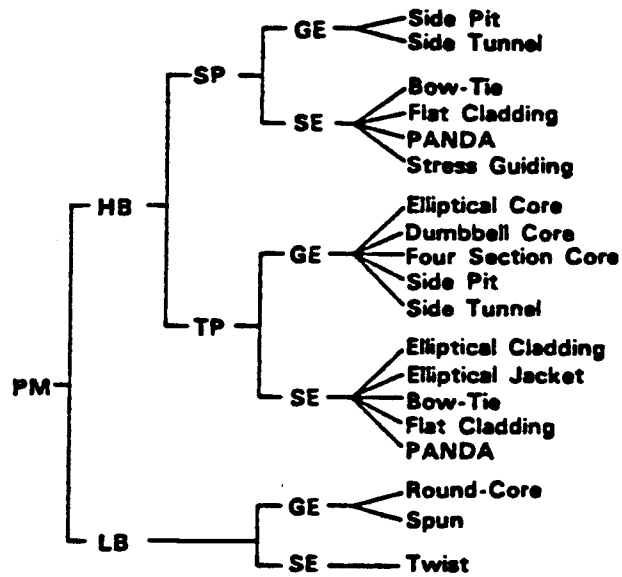

Fig. 1.1.b Kinds of polarization maintaining fibers classified from the linear polarization mainenance viewpoint. PM: Polarization Maintaining, HB: High Birefringent, LB: Low Birefringent, SP: Single Polarization mode, TP: Two Polarization modes, GE: Geometrical Effect, SE: Stress Effect

1.2 Waveguide Theory

Although the ray picture of light propagation through a fiber explains some of the observed properties, it is only an approximation for dimensions large compared to the wavelength of the light. Particularly for single mode fibers, where the core size is on the order of the wavelength, it is necessary to use wave optics to get a better description of the light propagation.

The laws governing the propagation of light in optical fibers are Maxwell's equations. They can be combined to produce the wave equation[6]

$$\nabla^2 \vec{E}_{(r)} - \mu_0 \epsilon \cdot \frac{\partial^2 \vec{E}_{(r)}}{\partial t^2} = 0 \qquad (1.2.1)$$

for the electric field or the magnetic field $\underline{H}$ respectively. The electromagnetic field distributions that will propagate are obtained by application of the boundary conditions of the fiber in question. These allowed distributions of the electromagentic field are called the modes of a fiber.

For a cylindrical dielectric waveguide there is no exact analytical solution for the wave equation. For weakly guiding fibers, however, the electric field for cylindrical symmetry and propagation in z-direction can be written as

$$\vec{E}_{(r,\varphi,z,t)} = \vec{E}_{(r,\varphi)} \cdot \exp[i(\omega \cdot t - \beta \cdot z)] \qquad (1.2.2)$$

where β is the longitudinal propagation constant of the wave inside the waveguide. The scalar wave approximation can be applied to transform

Maxwell's equations in cylindrical coordinates into the scalar wave equation [1]

$$\left[\frac{\partial^2}{\partial r^2} + \frac{1}{r}\cdot\frac{\partial}{\partial r} + \frac{1}{r^2}\cdot\frac{\partial^2}{\partial \varphi^2} + (k^2 n_j^2 - \beta^2) \right]\cdot E_z = 0 \qquad (1.2.3)$$

where n_j is equal to n_1 in the core and n_2 in the cladding. The equation for the magnetic field H_z is equivalent.

From (1.2.3) it follows that the field variations along r will always exhibit sinusoidal behavior when $(k^2 n_j^2 - \beta^2)>0$, and exponential behavior when $(k^2 n_j^2 - \beta^2)<0$. For a mode to be confined and guided by the fiber, however, the field has to be oscillatory in the core and exponentially falling off in the cladding. Thus the propagation constant is restricted to the interval

$$k\cdot n_2 \leq \beta \leq k\cdot n_1 \qquad (1.2.4)$$

where k is the wave number in free space and n_1 and n_2 are the indices of refraction of core and cladding, respectively $(n_1>n_2)$. Defining the parameters [1]

$$u = a\cdot(k^2 n_{co}^2 - \beta^2)^{\frac{1}{2}} \qquad (1.2.5a)$$

[transverse propagation constant]

$$v = a\cdot(\beta^2 - k^2 n_{c1}^2)^{\frac{1}{2}} \qquad (1.2.5b)$$

[transverse decay constant]

with a being the core diameter, the mode field $E(r,\varphi)$ obtained by plugging (1.2.2) into (1.2.3) can be expressed in terms of Bessel

functions $J(u\cdot r/a)$ inside the core and modified Hankel functions $K(v\cdot r/a)$ outside the core. The quadratic summation leads to a third parameter

$$V = u^2+v^2 = a^2k^2\cdot(n_{co}^2-n_{c1}^2) = (k\cdot a\cdot NA)^2 \qquad (1.2.6)$$

where NA is the numerical aperture as defined before. This is called the normalized frequency which depends only upon the wavelength of the incoming light and the fiber characteristics. The boundary conditions are that E_z, H_z and their normal radial derivatives must be continuous at the core-cladding interface. Incorporating these conditions in (1.2.3) leads to a relation $v=f_{(u)}$; and, together with (1.2.6), u and v can be determined graphically. This in turn defines the propagation constant β of the excited mode as a function of the frequency of the incoming light.

The low order modes propagating in a fiber and their propagation constants as a function of the normalized frequency are shown in Fig.1.2.a.[4] Due to the restrictions of β mentioned earlier, all except the fundamental mode HE_{11} have a cut off frequency below which they are not supported anymore. In order to get single mode characteristics therefore it is necessary to choose fiber geometry and wavelength such that $V<2.405$.

In the weakly guiding approximation,[3] the exact solutions of the waveguide theory, HE_{mn}, can be replaced by a set of modes which are linearly polarized, called LP_{mn} modes. The subscripts m and n give the number of azimuthal and radial nodes, respectively. This allows identification of the intensity pattern of the outcoming beam in a

multimode fiber. The fundamental mode, LP_{01}, has no azimuthal nodes, and consequently the outcoming beam has the shape of circular spot. From the exact solution, it is found that the radial field distribution of the fundamental mode is approximately Gaussian. The Gaussian width parameter is [1]

$$w_0 = a \cdot [0.65 + 1.619 \cdot V^{-1.5} + 2.879 \cdot V^{-6}] \qquad (1.2.7)$$

where w_0 is the radius of the $1/e^2$ intensity in the radial distribution. This is also the beam characteristics of a single mode fiber and will be used later in this study.

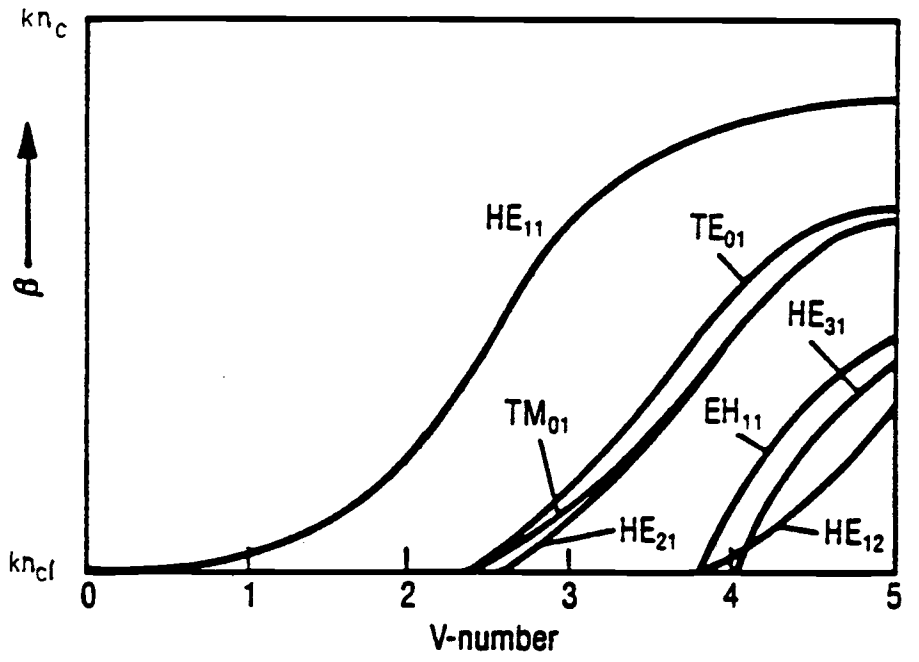

Fig. 1.2.a Low order modes of an optical single mode fiber

2. Mathematical Treatment of Optical Systems

2.1 Birefringence Effects: General Theory

In its broadest sense, the term birefringence refers to the anisotropy of dispersion in a medium. The birefringence is caused by the asymmetric internal arrangement and strength of the molecular binding forces. Birefringence can also be induced externally via asymmetric pressure, strain or applied electromagnetic fields. These stimulii cause a difference in the dispersion and therefore different refractive indices, $n(\omega)$, for two orthogonal states of polarization. The dependence of the refractive index upon frequency for two orthogonal polarization states in an anisotropic medium is shown in Fig.2.1.a.[4] It is seen that at a given frequency those two states have different indices of refraction. Regions where $dn/d\omega < 0$ correspond to absorption bands. This gives rise to the selective absorption of one of the two orthogonally polarized eigenstates of an incident beam. This effect is called dichroism and is used in polaroids to produce linearly polarized light.

The two basic birefringence effects are linear and circular birefringence, the latter is also called optical activity. The simplest linearly birefringent medium is a uniaxial crystal which has a preferred direction called the optic axis.
A linearly birefringent medium has different indices of refraction along two axis causing the polarized incoming light to be resolved into two orthogonal linearly polarized eigenstates, called the $\mathcal{P}$ states.

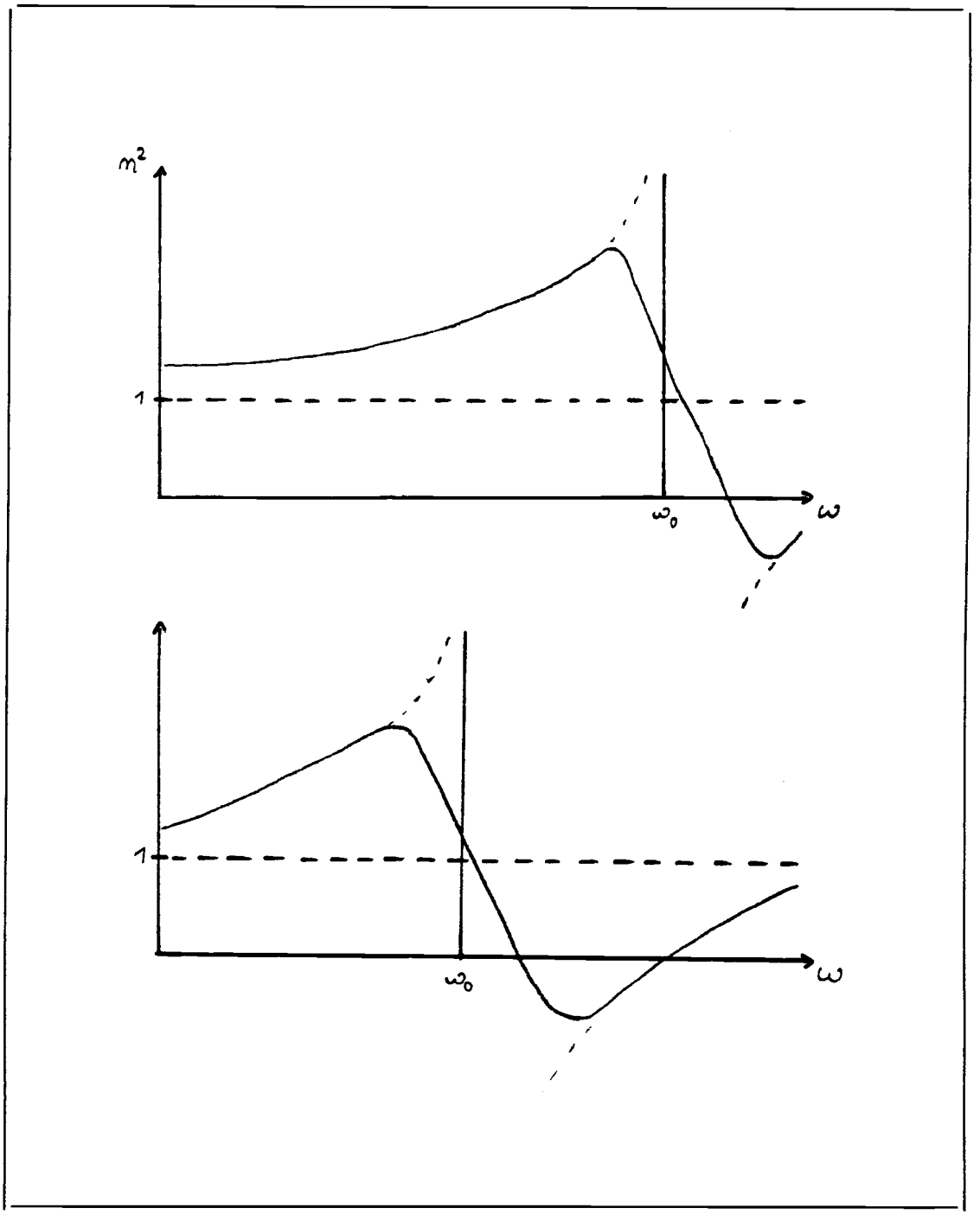

Fig. 2.1.a Refractive index versus frequency for two orthogonal states of polarization

Due to the different dispersion this introduces a phaseshift or retardation among the eigenstates which can be observed as a change in the state of polarization (SOP). A circularly birefringent medium, however, provides different indices of refraction for circularly polarized light, causing a resolution of the incoming polarized light into left- and right-handed circularly polarized eigenstates, called the $\mathcal{L}$ and $\mathcal{R}$ states. Introducing a retardation between those, however, doesn't change the SOP but rather rotates the entire state in its reference frame.

The most general case of birefringence, finally, is elliptical birefringence which can be thought of as being a superposition of linear and circular birefringence. Thus the polarized light gets resolved into two orthogonally elliptical SOP's which superpose to a changed and rotated SOP. The evolution of polarization in birefringent media can be described by Jones 2×2 matrix calculus which is the subject of the following sections of this chapter.

The most important electro-optical effects are the Kerr and Pockels effects, where the index of refraction along the direction of an applied dc electric field depends upon its magnitude quadratically or linearly, respectively. The magnetooptic-optic effect of interest in the present study is the induced circular birefringence or optical activity due to an external magnetic field.

For circular birefringence to occur, the medium must provide different indices of refraction for $\mathcal{L}$ and $\mathcal{R}$ states. This can be caused by some kind of circular molecular structure, for example left- and right-hand wound helices formed by long organic molecules. The Faraday

effect, however, depends upon the atomic and molecular energy levels rather then the form of the molecules. The following describes a classical picture which gives a good understanding of the Faraday effect.[4]

Suppose the incident light to be linearly polarized. In a circularly birefringent medium this will be resolved into $\mathcal{L}$ and R states. The circular states force the atomic bound electrons of the material to rotate in the opposite direction as the light does. An external magnetic field applied in the same direction as the light propagates, on the other hand, causes a Lorentz force acting radially on the rotating electron. Dependent upon the direction of the rotation and the magnetic field, the Lorentz force will tend to expand or compress the orbit of the electron, which gives rise to an induced polarization for the $\mathcal{L}$ state that is different than that for the R state. For a given magnetic field, therefore, there will be two different indices of refraction, causing the Faraday effect.

In the case of no other birefringence effects, the rotation F of the SOP depends upon the magnetic flux density H and the propagation distance L in the medium

$$F = V \cdot \int \vec{H} \cdot dl \qquad (2.1.1)$$

where V is a constant of the medium, called the Verdet constant. The Verdet constant for a particular medium varies with frequency and temperature and is of the order of 10^{-5} rad/gauss/cm for gases and

10^{-2} rad/gauss/cm for solids and liquids. For the study of the Faraday effect in a fiber the Verdet constant of fused silica, $V=1.6\times10^{-2}$ rad/gauss/cm, will be used.

As mentioned before, equation (2.1.1) only holds in the absence of other birefringence effects. These can be included by using the matrix description developed by R.C.Jones, where the Faraday effect is treated as an additional circular birefringence which can be obtained from the Faraday rotation by [5]

$$\alpha = 2 \cdot F \qquad (2.1.2).$$

2.2 Jones Matrix Description

Jones calculus is a matrix notation used to obtain a relation between the incoming and outgoing SOP as a function of the linear and circular retardation.[7] For polarized light the electric field can be written as

$$\begin{aligned}\vec{E} &= [\underline{i}E_{0x}\cdot\exp(i\varphi_x) + \underline{j}E_{0y}\cdot\exp(i\varphi_y)]\cdot\exp[i(kz-\omega t)] \\ &= \underline{E}_0\cdot\exp[i(kz-\omega t)] \end{aligned} \qquad (2.2.1)$$

where $\underline{E}_0$ is the complex amplitude which defines the SOP. The effect of birefringence is to change the complex amplitude which can be expressed as [7]

$$\underline{E}_0' = M\underline{E}_0 \qquad (2.2.2)$$

or

$$\begin{bmatrix} E_x' \\ E_y' \end{bmatrix} = \begin{bmatrix} m_1 & m_4 \\ m_3 & m_2 \end{bmatrix} \begin{bmatrix} E_x \\ E_y \end{bmatrix} \qquad (2.2.3)$$

The light propagation properties of a medium can be described by three fundamental types of optical elements, the linear polarizer, the partial polarizer and the rotator. Each of these elements can be represented by a 2×2 matrix acting as operators on the SOP. The linear retarder can be written in the form [7]

$$G = \begin{bmatrix} \exp[i\gamma] & 0 \\ 0 & \exp[-i\gamma] \end{bmatrix} \cdot \exp[i\varphi] \qquad (2.2.4)$$

where $\gamma=\frac{1}{2}(k_x-k_y)\cdot z$. Usually only the phase difference is of interest so that the phase factor $\varphi=\frac{1}{2}(k_x+k_y)\cdot z$ may be omitted. The treatment of the partial polarizer is very similar. The corresponding matrix is given by

$$P = \begin{bmatrix} p_1 & 0 \\ 0 & p_2 \end{bmatrix} \cdot \exp(i\varphi) \qquad \begin{matrix} 0 \le p_1 \le 1 \\ 0 \le p_2 \le 1 \end{matrix} \qquad (2.2.6)$$

For a perfect polarizer, therefore one of the p's will be zero. Both of these elements will be used to describe any kind of linear birefringence and since an optical fiber doesn't have significant absorption in either direction, the partial polarizer won't be of great importance in this study. The third fundamental element, the rotator, can be written as

$$S(\omega) = \begin{bmatrix} \cos\omega & -\sin\omega \\ \sin\omega & \cos\omega \end{bmatrix} \qquad (2.2.7)$$

which simply represents a rotation of the coordinate system, describing any kind of circular birefringence.

For multi-element systems the corresponding matrix can be found by multiplication of the individual element matrices

$$\underline{E}_n = M_n M_{n-1} \ldots\ldots M_2 M_1 \underline{E}_0 = M^{(n)} \underline{E}_0 \qquad (2.2.8)$$

with $M^{(n)}$ being the system matrix.

2.3 The Coupling of Linear and Circular Birefringence

The previous description of birefringence is applicable only if the system-elements behave either like a linear retarder or a rotator. If both local linear and circular birefringence are present the superposition gives rise to a local elliptical birefringence which is a function of position in the medium. This local coupling can be described by either of the following representations:

The Poincaré Sphere representation [10]

The differential Jones calculus [9]

The Poincaré Sphere is shown in Fig 2.3.a.[11] Poincaré expresses the ratio of the two complex components of the light in the form [7]

$$E_y/E_x = \xi+i\eta \qquad (2.3.1)$$

where ξ and η define the shape and orientation of the polarization ellipse. The Poincaré Sphere is the stereographic projection of the ξ,η plane onto a sphere of unit radius to which the plane is tangent at the origin of coordinates. Therefore each point on the sphere represents a SOP. The equatorial line represents linear SOP's including the origin of coordinates, the poles are circular $\mathcal{L}$ and R states and any other position vector represents elliptical polarization. In a birefringent medium the SOP undergoes a cycle of changes which traces out a closed trajectory $C_{(z)}$ on the sphere. For linear, circular and elliptical birefringence, these trajectories are circles with the eigenstate as its center. The position vector of the

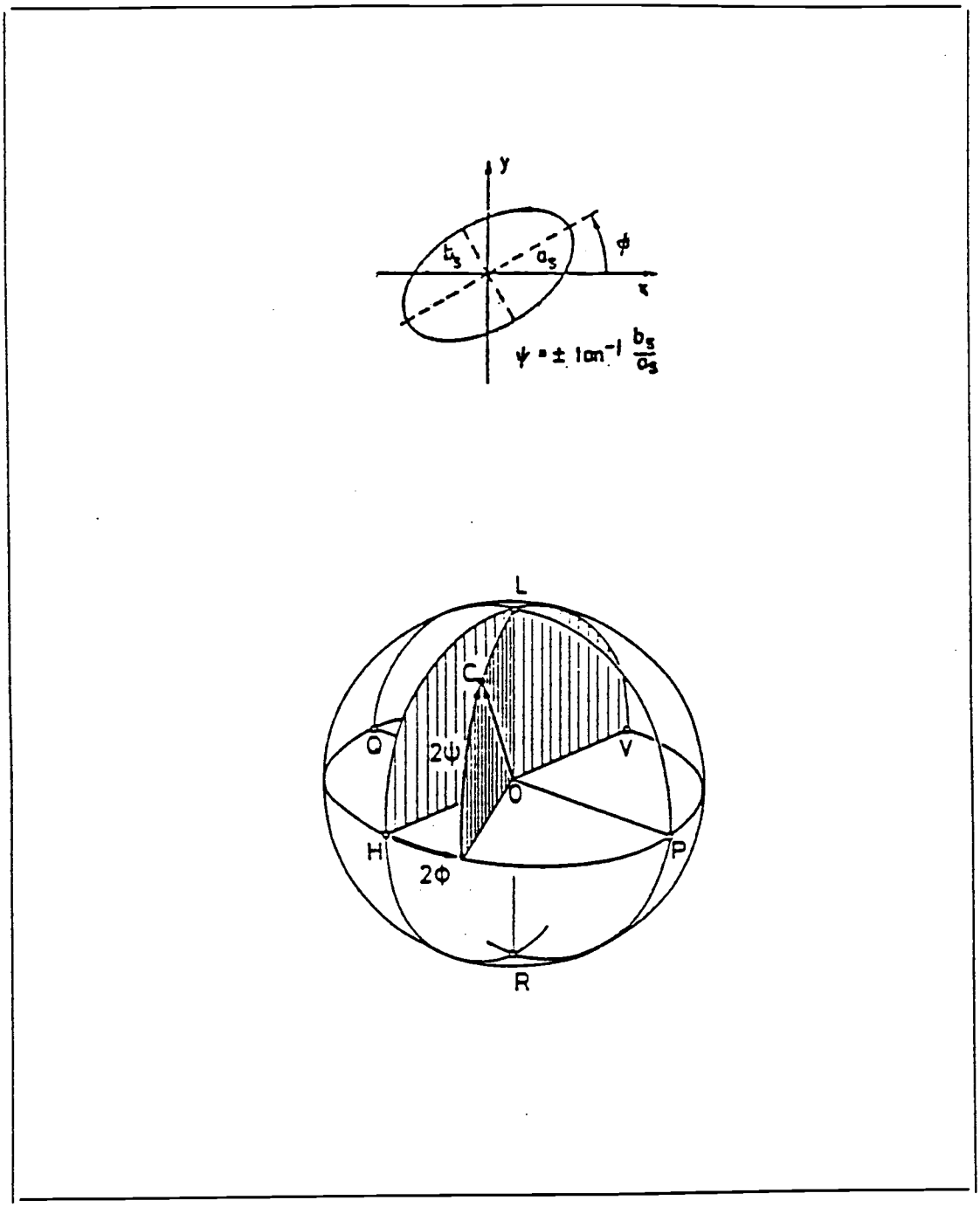

Fig. 2.3.a The polarization ellipse and its relation to the Poincaré Sphere

eigenstate represents the birefringence. Any elliptical birefringence can be resolved into a linear and a circular component. In the most general case of local birefringence as a function of position z in the medium, the resulting elliptical birefringence is found to be [11]

$$\vec{\omega}_{(z)} = \vec{\beta}_{(z)} + \vec{\alpha}_{(z)} \tag{2.3.2}$$

and

$$\omega^2_{(z)} = \beta^2_{(z)} + \alpha^2_{(z)} \tag{2.3.3}$$

with $\vec{\beta}_{(z)}$ and $\vec{\alpha}_{(z)}$ being the linear and circular birefringence, respectively. The z dependence, however, makes the evolution $C_{(z)}$ very complicated by the fact that the birefringence vector $\vec{\omega}_{(z)}$ itself is moving on the Poincaré sphere.

In cases without z-dependence the birefringence is called straight elliptical and the evolution of polarization can be represented by a rotation of the sphere about a fixed axis.

While the Poincaré Sphere gives a good illustration of the evolution of polarization, it takes the differential formulation of Jones calculus [9] to evaluate the SOP as a function of z, where the local change of the SOP is given by

$$d\underline{E}/dz = N\underline{E}. \tag{2.3.4}$$

where N is the differential system matrix. If there is no absorption the N-Matrix can be written as

$$N = \frac{1}{2} \cdot \begin{bmatrix} i\beta & \alpha \\ -\alpha & -i\beta \end{bmatrix} \tag{2.3.5}$$

where β, α are the magnitudes of linear and circular birefringence, respectively. This description is equivalent to the coupled mode theory, since two coupled mode equations can be obtained by factoring out equation (2.3.4). The system matrix M finally can be found by the integration of

$$dM/dz = NM \tag{2.3.6}$$

which yields [9]

$$M = \exp(N \cdot z). \tag{2.3.7}$$

For no z-dependence in α and β the eigenvalues of N,

$$\lambda_{1,2} = \pm \frac{i}{2} \cdot (\alpha^2+\beta^2)^{\frac{1}{2}} \tag{2.3.8}$$

are independent of z as well, and the coupled mode equations can be written as [19]

$$d^2\underline{E}/dz^2 = -\Gamma^2\underline{E} \tag{2.3.9}$$

where $\Gamma = \frac{1}{2}(\alpha^2+\beta^2)$. The solutions to equation (2.3.9) give the system matrix M for the coexistence of homogeneous linear and circular birefringence

$$\underline{E} = M\underline{E}_0 \tag{2.3.10}$$

where

$$M = \begin{bmatrix} \cos(\Gamma z) + \frac{1}{2} i\beta \cdot \frac{\sin(\Gamma z)}{\Gamma} & \frac{1}{2}\alpha \cdot \frac{\sin(\Gamma z)}{\Gamma} \\ -\frac{1}{2}\alpha \cdot \frac{\sin(\Gamma z)}{\Gamma} & \cos(\Gamma z) - \frac{1}{2} i\beta \cdot \frac{\sin(\Gamma z)}{\Gamma} \end{bmatrix}$$

(2.3.11)

The eigenmodes of this system are represented by the eigenvectors of M with the eigenvalues as their propagation constants. There are two special cases for the coupling of linear and circular birefringence:

case 1: homogeneous linear and circular birefringence

case 2: linear birefringence in a homogeneous twisted crystal

For these cases the resulting birefringence is straight elliptical without z-dependence which allows one to use the system matrix derived above.

case 1: homogeneous linear and circular birefringence

The M-Matrix derived above is valid with β and α being the sum of all linear and circular birefringences, respectively. The trajectories on the Poincaré sphere described are circles around the elliptical eigenstate. After the beat length [14]

$$L = 2\pi(\alpha^2+\beta^2)^{-\frac{1}{2}} \qquad (2.3.12)$$

the SOP's are reproduced.

case 2: linear birefringence in a homogeneously twisted crystal:

When the crystal is twisted,[12] the azimuthal angle ϕ of the linear birefringence β and the induced circular birefringence α are given by

$$\phi = \chi \cdot z \qquad \text{geometrical effect} \qquad (2.3.13)$$

$$\alpha = \chi \cdot g \qquad \text{elasto-optic effect} \qquad (2.3.14)$$

where χ is the twist rate and g is a material constant. Therefore the resultant elliptical birefringence becomes a function of z due to the z-dependence of β. However, describing the SOP in a reference frame which is rotating with the fiber twist removes the z-dependence in β and the circular birefringence transforms from

$$\alpha = \chi \cdot g \qquad (2.3.15)$$

to

$$\alpha = \chi \cdot (2-g) \qquad (2.3.16)$$

which can be substituted into (2.3.11) to get the system matrix. Again, other birefringence effects are just added and the beat length is given by equation (2.3.12).

3. The SM Fiber as an Optical System

3.1 Birefringence Effects in an Optical Fiber

The prerequisite for birefringence is an anisotropy in the medium. Since silica glass itself is isotropic, birefringence effects in an optical fiber are due to external stress, electromagnetic fields or the fiber geometry. The effects discussed in this section are the core shape, external pressure, bending, twist and the Faraday effect.

a) The shape of the core

Due to imperfections in the fiber drawing process, the cross section of the core is not perfectly circular. This gives rise to the so called intrinsic linear birefringence. Methods to calculate the intrinsic birefringence using an elliptical core approximation are discussed in the literature.[1] As the manufacturing imperfections are random, there are no specifications for this effect available and the intrinsic birefringence must be determined for each fiber piece individually.

In chapter 5 a method is described to measure the intrinsic birefringence since its magnitude is of importance for the theoretical evaluation of a current sensor.

b) External pressure

The basic principle of a single-mode fiber optic pressure sensor is to measure the change of the SOP due to the pressure-induced stress.

For the present study it was important to be aware of this effect to avoid external pressure in the experimental setups.

c) Bend induced birefringence [16,17]

Stress induced birefringence due to bending is of great importance since many setups and devices involve fiber optic coils or helices. This birefringence results from the fiber core being deformed. In reference 17 it was found that the bend induced birefringence can be calculated by

$$\beta_b = \text{const.} \cdot \kappa^2 \cdot r^2 \qquad (3.1.1)$$

where κ is the fiber curvature and r the cladding radius. For a circular path the curvature is 1/R, R being the radius of the circle. The constant involved depends upon several material properties and the wavelength of the light. For fused silica at λ=633 nm this constant was found theoretically and by experiment to be -7.7×10^7 deg/m. This value should hold universally for weakly guiding silica fibers, regardless of their core diameters and index profiles.

d) Twist induced birefringence

In the twisted fiber, the strain-induced optical activity is proportional to the twist. According to reference 14 it is given by

$$\alpha = g \cdot \chi \qquad (3.1.2)$$

where χ is the twist rate and g is a material constant. This constant was calculated and measured to be g≈0.13-0.16 which should hold

universally for weakly doped single-mode fibers of arbitrary index profile.

d) The Faraday effect [15]

The basic theory for the Faraday effect is given in chapter 2.1. The Verdet constant V depends upon the material and the wavelength of the light and for silica glass it is typically 4.68×10^{-6}rad/A at λ=633nm. It should be mentioned, however, that this constant depends upon the doping of the fiber and the value given above is valid only for weakly doped fibers.

The Faraday effect can be included in the system matrix M for the coupling of linear and circular birefringence given in chapter 2.3 by treating it as an additional circular birefringence

$$\alpha = 2V\cdot\int \vec{H}\cdot d\vec{l} \qquad (3.1.3)$$

Since the distance traveled by the light in the fiber can be very long, a considerable rotation can be expected. This effect would allow fiber optics to be utilized as magnetic field sensors.

3.2 The Geometric Rotation

It has been discovered recently,[19-22] that there is another induced circular birefringence due to the spatial path of the fiber. This effect, the so called geometric rotation, is independent of the wavelength of the light and the fiber boundary conditions. The following theory has been developed by J.N. Ross in 1984 and uses classical electrodynamics and differential geometry to describe the effect.

There are two constraints on the lightwave as it travels through a single mode fiber:

a) The mode has to be preserved

b) The principle of constant azimuthal angle must be obeyed

a) The preservation of the mode

The modes, which are supported by the fiber, are determined by the boundary conditions inside the fiber. These do not depend upon the spatial path of the fiber and therefore the mode remains the same. This, on the other hand, means that the tangential component of the electric field is independent of z. We express this constraint by requiring a constant angle between the electric field and the tangent vector $\vec{t}$ of the fiber path.

b) The constant azimuthal angle

When the fiber is bent with a curvature κ at point P1, there is a plane of curvature which passes through the center of curvature and is

tangential to the curve at P1. The normal vector to this plane is called the binormal $\vec{b}$.

As recently discovered,[19] the angle between the binormal $\vec{b}$ and the electric field vector doesn't change as the light propagates along the fiber unless the curvature is very large, i.e. R< 1mm. This results from the validity of the parallel transport law[3] of the electromagnetic field vectors which can be derived classically by using Maxwell's equations in the weak guidance approximation. The experiment described in chapter 4 supports this theory and is taken as a manifestation of its validity.

The constraints a) and b) force the vectors $\vec{t}$, $\vec{E}$, and $\vec{b}$ to move as a vector-trihedral along the fiber. Using Gram-Schmidt orthonormalization to replace $\vec{E}$ by the normal vector to the fiber $\vec{n}$, which points towards the center of curvature, an orthonormal trihedral of vectors can be defined everywhere in the fiber. Fig.3.2.a shows the evolution of the vector-trihedral along the fiber.

The evolution of $\vec{n}$, $\vec{t}$, and $\vec{b}$ as a function of the curvature κ and the torsion τ is given by Frenet's Formulas, derived in differential geometry:[23]

$$\vec{t}' = d\vec{t}/ds = \kappa \cdot \vec{n} \qquad (3.2.1a)$$

$$\vec{n}' = d\vec{n}/ds = -\kappa \cdot \vec{t} + \tau \cdot \vec{b} \qquad (3.2.1b)$$

$$\vec{b}' = d\vec{b}/ds = -\tau \cdot \vec{n} \qquad (3.2.1c)$$

If the polarization is measured with respect to the binormal $\vec{b}$, a geometric rotaion can be observed if $\vec{b}$ changes, i.e if the fiber path

leaves its original plane of curvature. The orientation of the polarization θ_p at a point P with respect to the local binormal vector is related to the polarization orientation θ_0 at P_0 by [19]

$$\theta_p = \theta_0 - \int \tau \cdot ds. \qquad (3.2.2)$$

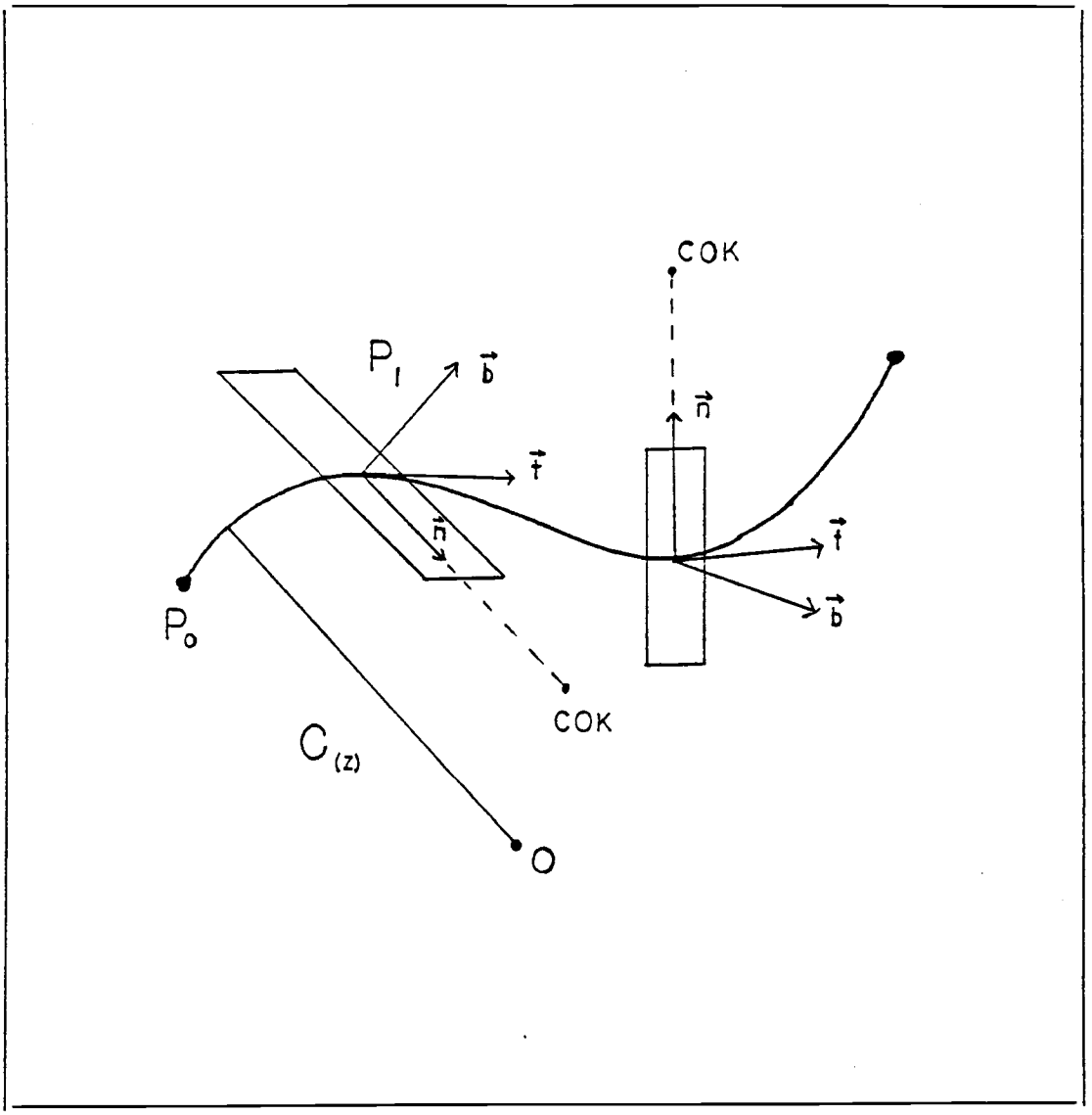

Fig. 3.2.a Evolution of the vector-trihedral along the fiber

When the fiber path is described by a position vector $\vec{r}$, which is a function of a general parameter t, we obtain the following expressions for the curvature and torsion:

$$\kappa^2 = |\vec{r}'\times\vec{r}''|^2/(\vec{r}'\cdot\vec{r}')^3 \qquad (3.2.3)$$

$$\tau = (\vec{r}'\vec{r}''\vec{r}'')/|\vec{r}'\times\vec{r}''|^2 \qquad (3.2.4)$$

where $\vec{r}'=d\vec{r}/dt$ and

$$(\vec{r}'\vec{r}''\vec{r}'') = \begin{vmatrix} r_1' & r_2' & r_3' \\ r_1'' & r_2'' & r_3'' \\ r_1'' & r_2'' & r_3'' \end{vmatrix} \qquad (3.2.5)$$

From a quantum mechanical treatment of the geometric rotation there is another way to calculate the orientation of the polarization which is equivalent to the one above.[20] It is derived from the statement, that the angle of rotation is equal to the solid angle on the unit sphere subtended by the $\vec{k}$ vector of the photon as it changes its direction adiabatically due to the guidance of the fiber. The normalized $\vec{k}$ vector of the photon on the other hand is the same as the normalized tangent vector of the fiber curve, which is given by

$$\vec{T}_{(t)} = \vec{r}'/|\vec{r}'| \qquad (3.2.6).$$

As it is shown in Fig. 3.2.b, $\vec{T}(\varphi_{(t)})$ traces out a path $C(\varphi_{(t)})$ on the unit sphere and the solid angle $\Omega_{(C)}$ is the enclosed area which can be found by the integration in spherical coordinates of

$$\Omega_{(C)} = \int_0^{2\pi}\int_0^{\theta} \sin\theta^* \, d\theta^* \, d\phi = \int_0^{2\pi} \{1-\cos\theta(\phi)\} d\phi$$

$$= \int_0^{2\pi} \{1-\cos\theta(\phi)\} \frac{d\phi}{dt} \cdot dt = \int_0^{2\pi} \{1-\cos\theta_{(t)}\} \phi'_{(t)} dt \qquad (3.2.7)$$

where

$$\phi_{(t)} = \arctan\left[\frac{T_y}{T_x}\right] \qquad (3.2.8)$$

$$\phi'_{(t)} = \frac{T'_y T_x - T'_x T_y}{T_x^2 + T_y^2} \qquad (3.2.9)$$

$$\theta_{(t)} = \arccos\left[\frac{T_z}{T}\right] \qquad (3.2.10)$$

In the following paragraph these calculations are performed for the geometry of a straight and toroidal helix which will be needed in chapter 4 and 5.

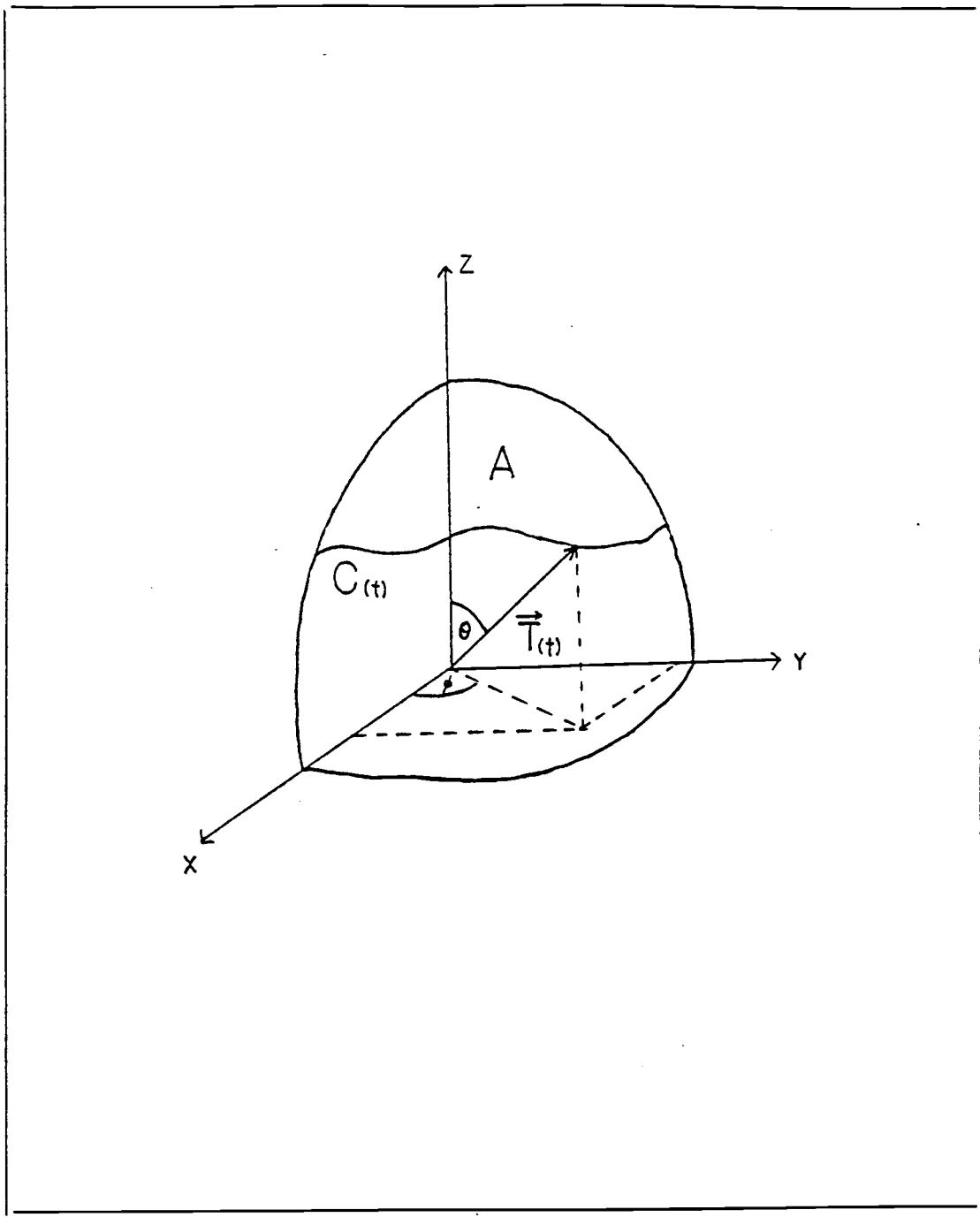

Fig. 3.2.b Path $C_{(t)}$ traced out by the tangent vector of the curved fiber and the solid angle as the enclosed area A

3.3 Special Geometries

The previous theory is applied to find the geometric rotations for the following geometries

a) The uniform helix including one harmonic deformation

b) The helix wrapped on a toroid

as shown in Fig.3.3.a. Geometry a) will be used in chapter 4 to verify the geometric rotation, geometry b) represents the magneto optic current sensor investigeted in chapter 5.2. In both cases it turned out to be easier to evaluate the geometric rotation through the solid angle subtended by the tangent vector of the curve on the unit sphere.

a) The uniform helix and one harmonic deformation

Fig.3.3.b shows an example for the curve of a uniform helix and one harmonic deformation of amplitude A. The vertical axis represents $r \cdot \phi$, where r is the cylinder radius and ϕ the azimuthal angle of the point on the cylinder, the horizontal axis is the z axis. For the uniform helix the local pitch angle $\theta(\phi)$ is constant and

$$\cos\theta(\phi) = p/s \qquad (3.3.1)$$

where p is the pitch and s the length of the fiber

$$s = [p^2 + (2\pi r)^2]^{\frac{1}{2}} \qquad (3.3.2).$$

Since for the uniform helix p does not depend upon ϕ, θ is constant as well and the path traced out by the tangent vector on the sphere is

simply a circle, as shown in Fig. 3.3.b. The solid angle subtended by the closed path C with respect to the center of the sphere

$$\Omega_{(C)} = \int_0^{2\pi} [1-\cos\theta(\phi)]d\phi \qquad (3.3.3)$$

therefore reduces to

$$\Omega_{(C)} = 2\pi\cdot(1-p/s). \qquad (3.3.4)$$

This predicts a circular rotation of

$$\gamma_{(C)} = -\sigma\cdot\Omega_{(C)} = -2\pi\cdot[1-p/s] \qquad (3.3.5)$$

where the helicity σ=-1. Since equation (2.3.3) is only valid for C being closed, the input and output lead of the fiber helix have to be parallel. This is the case in all the geometries under consideration. For one harmonic deformation, however, the calculations are somewhat more complicated. One harmonic deformation is defined to be the path given by the equation

$$z/r = (\tfrac{1}{2}p\pi r)\cdot\phi + A\cdot\sin\phi \qquad (3.3.6)$$

where A is the degree of deformation. This can be used to find the curve on the paper wrapped around the cylinder. Since $\theta(\phi)$ now depends upon ϕ, the integral (3.3.3) becomes

$$\Omega_{(C)} = \int_0^{2\pi} \{1-\cos[\tan^{-1}\left[\frac{r}{\frac{1}{2}\pi p + \text{Arcos}\phi}\right]]\}\, d\phi \qquad (3.3.7)$$

which must be solved numerically to determine $\gamma_{(c)}$. The results are presented in chapter 4.2.

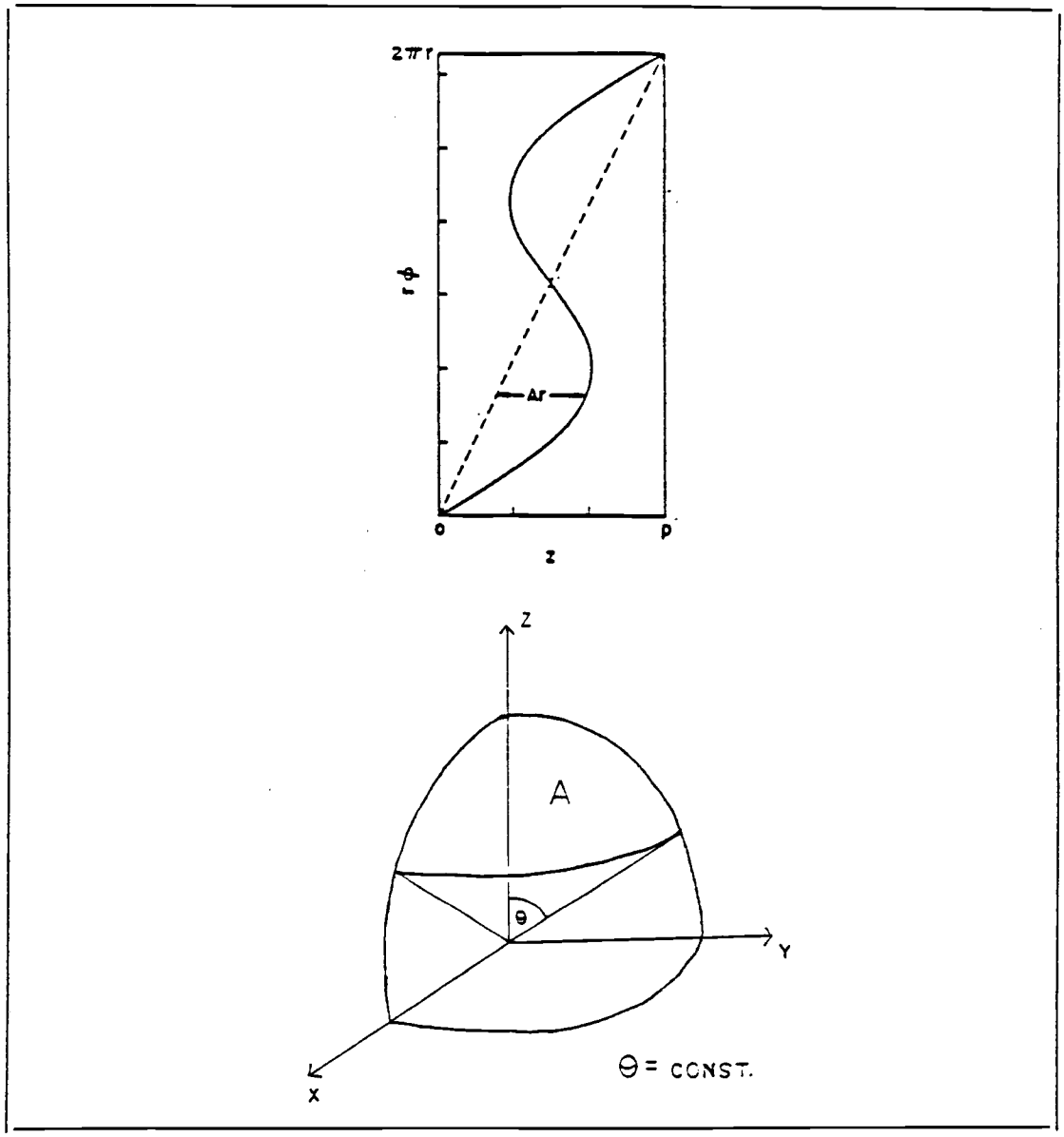

Fig. 3.3.b Top: Curve of a uniform helix (dashed line) and one harmonic deformation of amplitude A=1.2 (solid line). The lines represent the path of the fiber on an unwrapped cylinder surface; Bottom: Path traced out by the tangent vector on the unit sphere for a uniform helix.

b) Helix wrapped on a toroid

The curve of a helix on a toroid is given as a function of the parameter t

$$C_{(t)} = [x_{(t)}, y_{(t)}, z_{(t)}] = \vec{r}_{(t)} \tag{3.3.8}$$

with

$$x_{(t)} = (R + r\cos(Nt))\cdot\cos(Nt) \tag{3.3.9a}$$

$$y_{(t)} = (R + r\cos(Nt))\cdot\sin(Nt) \tag{3.3.9b}$$

$$z_{(t)} = r\cdot\sin(Nt) \tag{3.3.9c}$$

where N is the number of turns on the toroid and R, r, and t are defined as shown in Fig. 3.3.c. Using equation (3.2.6) the tangent vector is given by

$$\vec{T} = \frac{[dx/dt, dy/dt, dz/dt]}{T} = \frac{[x', y', z']}{N\cdot[R^2+r^2+2rR\cos(Nt)+r^2\cos^2(Nt)]^{\frac{1}{2}}} \tag{3.3.10}$$

where

$$\begin{bmatrix} x' \\ y' \\ z' \end{bmatrix} = N\cdot\begin{bmatrix} -R\sin(Nt)-2r\cos(Nt)\sin(Nt) \\ R\cos(Nt)-r\sin^2(Nt)+r\cos^2(Nt) \\ r\cos(Nt) \end{bmatrix} \tag{3.2.11}$$

Using equation (3.2.9) we obtain

$$\phi'_{(t)} = N\cdot\frac{R^2+2r^2+3Rr\cos(Nt)}{R^2+r^2+2Rr\cos(Nt)} \tag{3.3.12}$$

and the substitution of (3.2.10) and (3.3.12) into (3.2.7) yields

$$\Omega_{(c)} = \int_0^{2\pi} dt\cdot N\cdot\frac{R^2+2r^2+3Rr\cos(Nt)}{R^2+r^2+2Rr\cos(Nt)}\cdot\left[1-\frac{r\cos(Nt)}{[R^2+r^2+2rR\cos(Nt)+r^2\cos^2(Nt)]^{\frac{1}{2}}}\right] \tag{3.3.13}$$

This integral has been evaluated numerically using Simpson's rule. The results of interest for this study are presented in chapter 5. The length of the fiber for one cycle around the toroid is given by

$$s = \int ds = \int_0^{2\pi} \left|\frac{d\vec{r}}{dt}\right| dt = \int_0^{2\pi} |\vec{T}| \, dt \qquad (3.3.14)$$

With equation (3.2.3) the curvature of the path as a function of t is given by

$$\kappa^2 = |\vec{r}'\times\vec{r}''|^2/(\vec{r}'\cdot\vec{r}')^3 \qquad (3.2.3)$$

where

$$|\vec{r}'\times\vec{r}''|^2 = \{(r^2\sin^3(Nt)+3r^2\cos^2(Nt)\sin(Nt))^2 + \\ + (Rr+2r^2\cos^3(Nt))^2 + (R^2+2r^2+3Rr\cos(Nt))^2\}^3 \qquad (3.3.15)$$

and

$$(\vec{r}'\cdot\vec{r}')^3 = \{(R\sin(Nt)+2r\sin(Nt)\cos(Nt))^2 + \\ + (R\cos(Nt)+r\cos^2(Nt))^2 + r^2\cos^2(Nt)\}^3 \qquad (3.3.16)$$

These equations for the curvature will be used in chapter 5 to find the bend induced birefringence in an optical fiber having this geometry. In order to find the path $C(\phi)$ traced out by $\vec{T}$ on the unit sphere analytically it is necessary to combine equations (3.2.8) and (3.2.10) to obtain the function $\theta(\phi)$. For the tangent vector given in (3.3.10) this seems to be impossible and a numerical method was used to find the path shown in Fig.3.3.c., calculated for the parameters R=0.08m and r=0.018m.

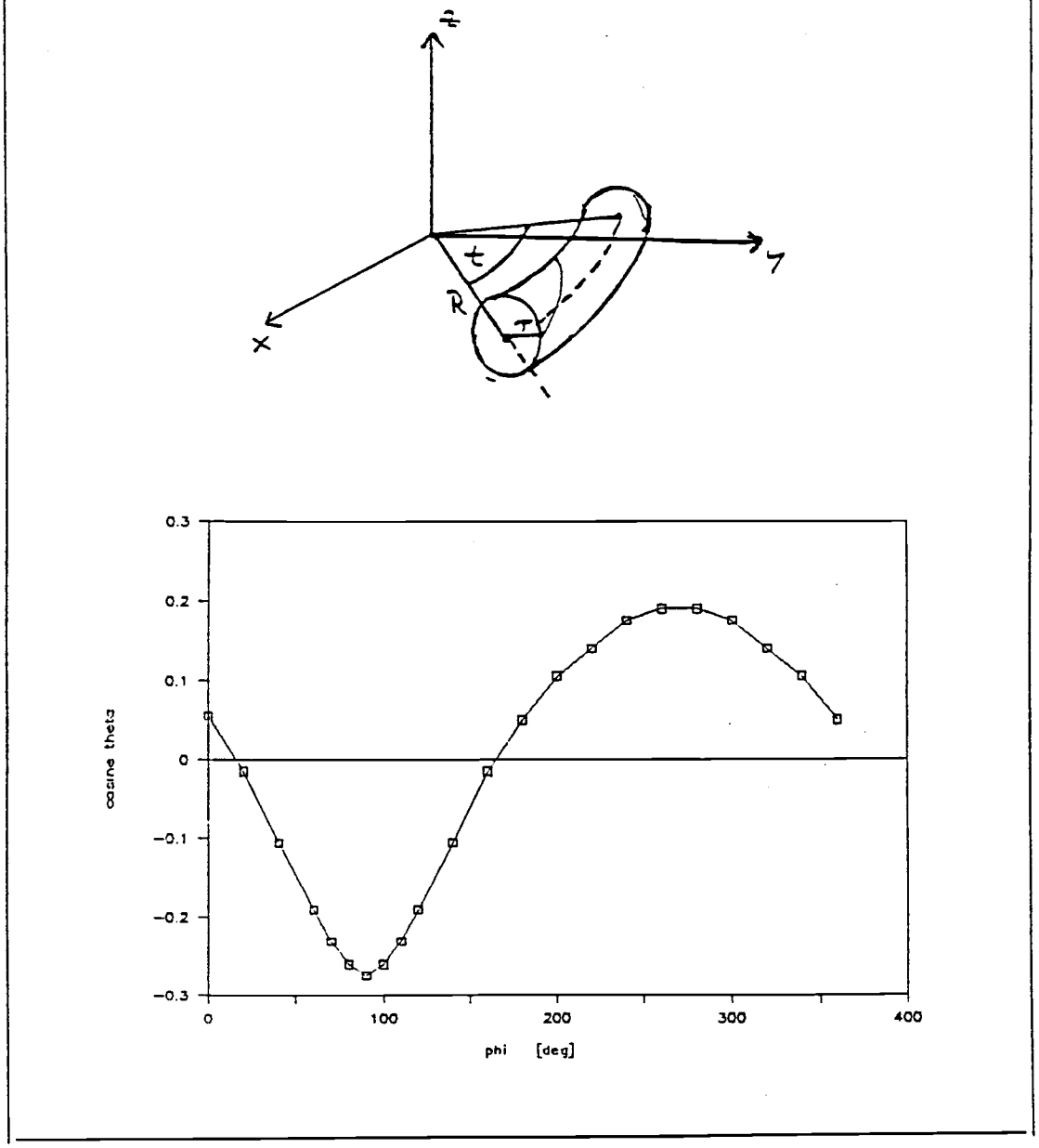

Fig.3.3.c Top: Parameters used to evaluate the geometric rotation of the helix on a toroid, Bottom: Path traced out by the tangent vector on the unit sphere for N=1. The y-axis represents cos $\theta(\phi)$, the x-axis represents ϕ in degrees, where θ and ϕ are spherical coordinates.

4. Experimental Manifestation of the Geometrical Effect

4.1 The Experiment

The objective of this experiment was to measure the rotation of linearly polarized light due to the spacial geometry of the guiding fiber path. Uniform helices of different pitch and radius were investigated as well as single harmonic deformations. Detailed description of the geometries and theoretical calculations were given in chapter 3.3. The results of the theoretical calculations for the helix parameters used in this experiment appear in table 4.1.

The experimental setup is shown in Fig.4.1.a.[20]
A 5mW laser with linear input polarizer and analyzer were used to measure the rotation of the plane of polarization. With the direction of the polarization along the y-axis, the light was launched into the fiber by a focusing lens and x-y holder. The output was analyzed by the second polarizer which was rotated by the data acquisition system. A collimating lens was used to cover the active area of the sensing photodiode entirely. The digitized output of the amplified photocurrent was collected by an IBM-PC. A plot of the intensity versus angle of rotation of the analyzer was made. The position of the maximum and minimum intensities and therefore the rotation could be found graphically. Signal averaging was used to eliminate random noise A sample plot of the intensity curve is shown in Fig.4.1.b.

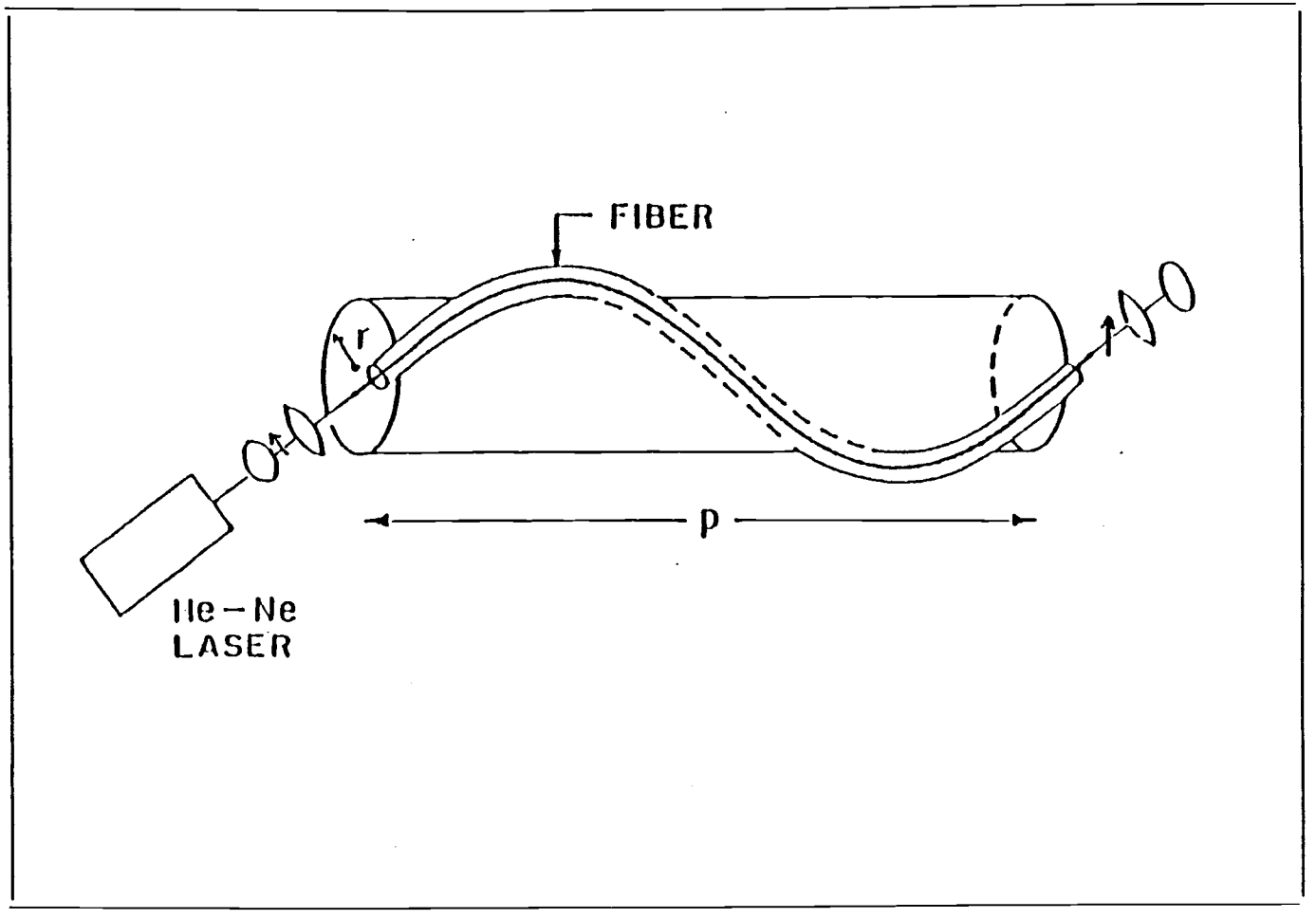

Fig.4.1.a The experimental setup

Specifications of the components:

Laser: 5 mW He-Ne laser, wavelength 633nm

Coupler: focusing lens with 30mm focal length and x-y fiber holder

Fiber: Newport single-mode fiber F-SV with silica core and cladding

core, cladding, coating diameter: 4μm, 125μm, 300μm

numerical aperture: NA= 0.11

V-number: V= 2.19 at 633nm

optimum wavelength 633nm, stepped index profile

The most delicate part of the experimental setup was the laser-fiber coupling. Prerequisite for efficient coupling was a careful preparation of the fiber ends. To remove the plastic coating the fiber end was soaked in methylene chloride for 3 minutes. Upon removal, the coating was easily wiped off. The crucial step in the preparation was cleaving the end. A flat end face without defects and perpendicular to the fiber axis is necessary for good coupling. This was achieved by scribing the cladding with a razor blade perpendicular to the fiber and then bending the fiber until it breaks. The small nick from the razor blade propagates through the fiber without introducing defects on the surface. A strong dependence of the coupling upon the cleave was observed and usually several tries were necessary to achieve a satisfactory result. Of similar importance is the proper alignment of the fiber to the focused incoming beam. First, the angle of the incoming beam has to be within the aperture. In addition, the incident electromagnetic field distribution has to match the profile of the mode propagated by the fiber, given by equation (1.2.6) for the HE_{11} mode

profile. The radius of the $1/e^2$ intensity point of the beam, w, can be calculated to be 2.35μm. This is the ideal size of the focused spot. The spot size of a focusing lens is given by [4]

$$w_f = \frac{4 \cdot \lambda \cdot f}{\pi \cdot r} \qquad (4.1.1)$$

where λ is the wavelength, f the focal length of the lens and r the incoming beam radius. For the lens used in this experiment the smallest spot size achievable can be calculated to be 3μm. This, unfortunately, is too large and therefore the coupling efficiency was not optimal. However, an estimated coupling of 30% was achieved which turned out to be sufficient to perform the experiment.

To ensure that the measured rotation was of topological nature only it was of great importance to avoid any other birefringence effects. These are in general due to external stress on the fiber. A quantitative analysis of these effects is given in section 4.2. For the experiment, however, it was important to avoid stress due to pressure, bending or twisting. Possible pressure points were mainly the fiber holders on both ends. The fiber was clamped between soft rubber plates with a guiding notch of the size of the fiber. In order to keep the twist rate small the fiber was insterted into a rubber tube large enough to guide the fiber losely. Since the bend induced birefringence depends upon $1/R^2$, where R is the radius of the curvature, the only way to avoid this is to work with large enough radii. A radius greater than 5cm was calculated to be reasonable.

Detection and Data Collection:

A negative biased photodiode measured the light intensity. The 8 bit A/D converter digitized the amplified signal to numbers between 0 and 255. Random fluctuations, mainly due to vibrations affecting the laser-fiber coupling, were removed through signal averaging. The software drove a steppermotor rotating the polarizer with 720 steps per rotation. 100 readings per step were found to be sufficient to yield a smooth sinusoidal curve. A sample plot is shown in Fig.4.1.b. The data points connected by the curve are one half of a degree apart due to the limited resolution of the graphics program used to draw the graph. The minimum or maximum positions on the 360° scale were used to find the angle of rotation. An uncertainty of ±3° in the measurement was considered in the data analysis in chapter 4.2.

4.2 Data Analysis

To verify the topological phase experimentally the measured values were compared to the theoretical prediction of the circular rotation. Simple paths of uniform helices were investigated as well as helices with one harmonic deformation. The paths on the cylinder were found by wrapping a paper with the calculated curve onto the cylinder as shown in Fig 3.3.b. Measurements were taken on three sheet metal cylinders of different radius and pitch. The following dimensions were investigated:

r_1=6.8cm, p_1=130cm; r_2=10cm, p_2=80cm; r_3=14cm, p_3=43cm.

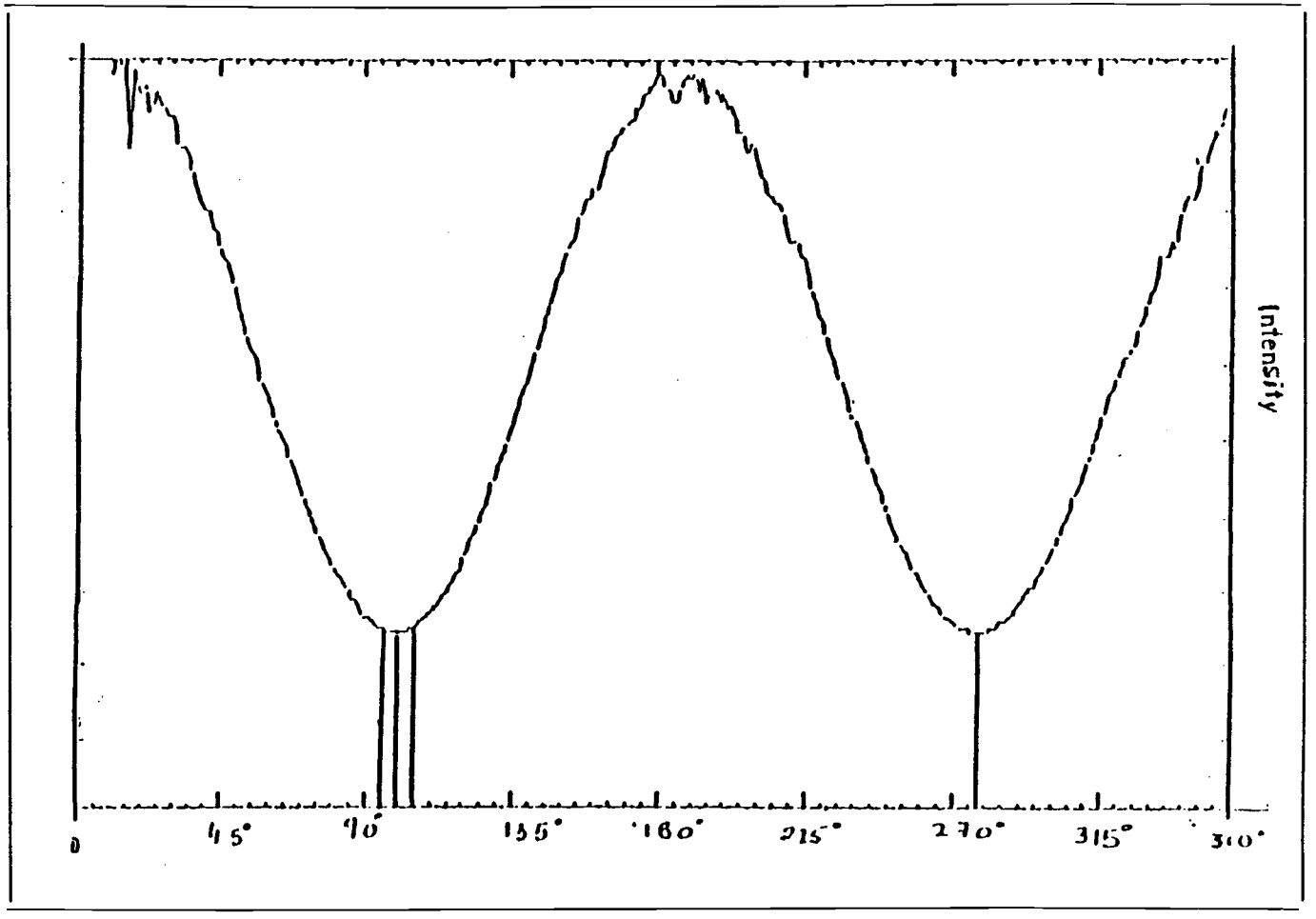

Fig.4.1.b Sample plot of the intensity curve

In each case measurents were taken for A=0, 0.3, 0.6, 0.9, 1.2.

Errors due to external stress were discussed quantitatively.

Table 4.2.I shows the experimental and calculated expected values for the angle of rotation for each cylinder and different degrees of deformation A.

Table 4.2.I

Measured and Calculated Values of the Rotation in Radians for Different Cylinders and Deformations

	r_1=6.8cm;p_1=130cm		r_2=10cm;p_2=80cm		r_3=14cm;p_3=43cm	
A	theory	experiment	theory	experiment	theory	experiment
0	0.27	0.31	1.27	1.37	3.45	3.51
0.3	0.25	0.35	1.42	1.54	3.90	3.95
0.6	0.40	0.38	1.83	1.87	4.40	4.38
0.9	0.45	0.43	2.15	2.22	4.45	4.50
1.2	0.62	0.50	3.15	3.10	5.22	5.10

Fig.4.1.c shows a plot of the theoretically calculated values for the rotation versus the measured results in radians. The data points +, *, □ are the measurements taken on cylinder 1, 2, and 3, respectively. As can be seen, the theoretical and experimental values agreed very well in almost all cases.

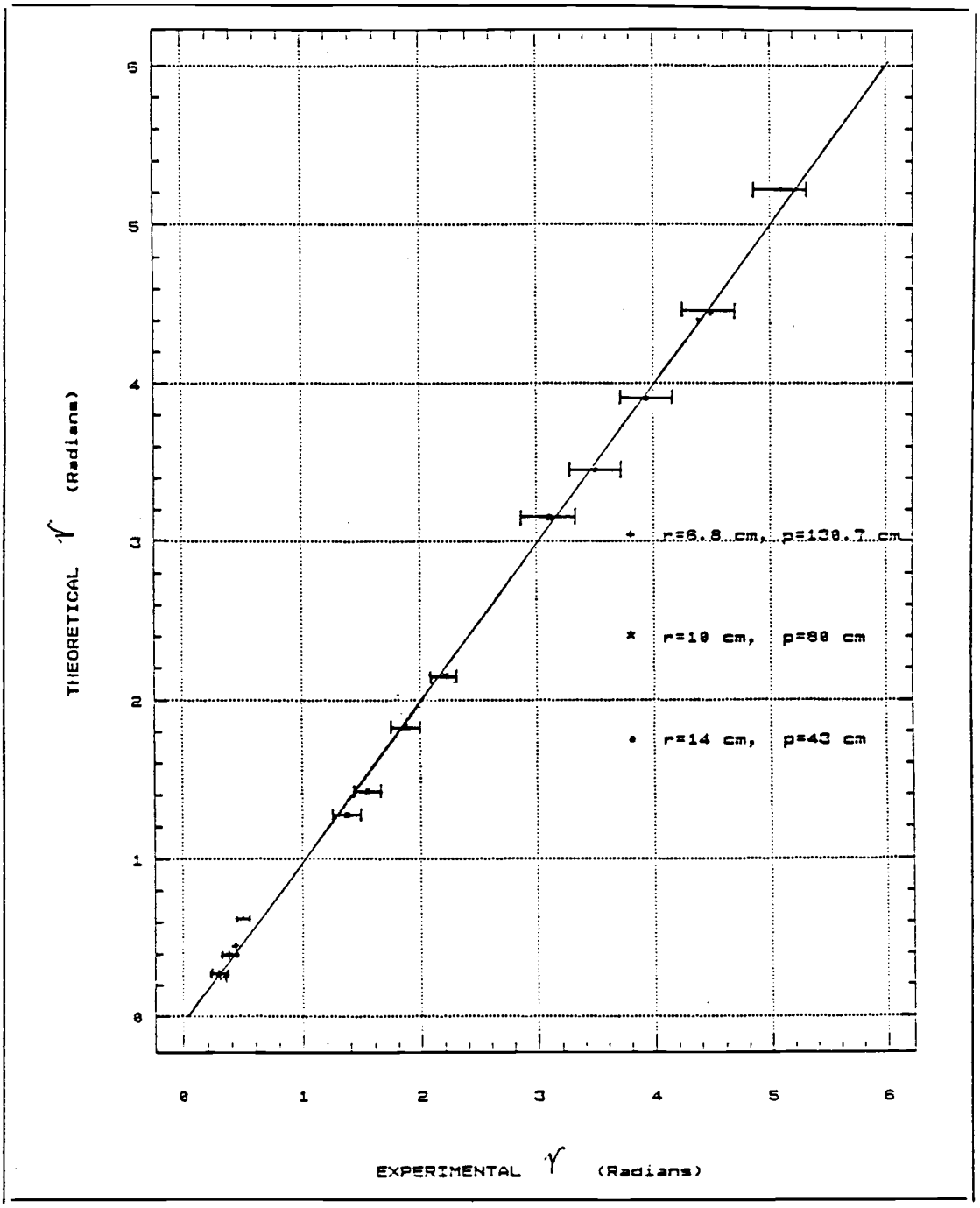

Fig.4.1.c Theoretical calculated values for the roatation versus the measured results in radians.

Error Bars:

In order to insure that the measured rotation is due to Berry's phase only it is necessary to get a quantitative estimation of the other birefringence effects present. This could have been intrinsic, pressure and bend induced linear birefringence as well as twist induced circular birefringence.

By measuring the influence of a straight fiber on linearly polarized light it was found that the intrinsic birefringence is negligible compared to the topological effect expected. This agreed with the classification of the fiber as being low birefringent by the producer. The other birefringence effects, however, can become significant if external stress is applied to the fiber. Pressure induced birefringence was kept small by careful preparation of the fiber holders. It was found that intentional introduced pressure at these points didn't effect the polarization at the end which led to the conclusion that this effect was negligible. Bend and twist induced birefringence on the other hand is not negligible. In chapter 3.1 the bend and twist induced birefringence are given with equations (3.1.1) and (3.1.2). Equation (3.2.3) in chapter 3.2 can be used to find the curvature of the fiber for a uniform helix of radius a and pitch $2\pi \cdot b$ to be [23]

$$\kappa = \frac{a}{(a^2+b^2)} \qquad (4.2.2)$$

The evaluation of the bend induced birefringence using eqs. (3.1.1) and (4.2.2) is shown in table 4.2.II. The contribution of the calculated

linear retardation to the rotation of the linear polarized light depends upon the angle of the incident light with respect to the major axes of the fiber. It is well known that these are parallel and perpendicular to the z-axes of the helix. For the polarization of the incoming light being parallel to one of these axes, its state of polarization will be the least affected by the linear birefringence. Due to the coupling between linear retardation and circular birefringence it would be necessary to use Jones calculation to get an exact value for the bend induced rotation. A good estimation however can be obtained by comparing the beat length of the linear birefringence with the length of the fiber. The beat length is given by

$$L_b = 2\pi/\beta \qquad (4.2.3).$$

Table 4.2.II shows the different beat lengths of the bend induced birefringence on the cylinders used.

Table 4.2.II

Bend Induced Birefringence on the Different Cylinders

	cyl 1	cyl 2	cyl 3
β_b [rad/m]	-.01	-.07	-.17
L_b [m]	628	90	37
$2\cdot\pi\cdot l/L_b$ [rad]	0.01	0.06	0.16
Relative error	≤4%	≤5%	≤5%

The ratio of the fiber length over the beat length gives the change of the state of polarization due to bend induced birefringence and multiplied by 2π it yields an upper limit for the rotation of the polarization ellipse. The values in table 4.2.II were obtained for the anharmonic deformation A=0. Since the topological rotation is increasing for higher A values, the errors can be assumed to be even smaller.

The other important stress effect present is the twist induced birefringence since due to equation (3.1.2) with g=0.13 even small twist rates contribute significantly to the rotation of the polarization. However, twist can be avoided by guiding the fiber loosely such that it can detwist. This was done by inserting the fiber into a rubber tube.

Looking at the ease of moving the fiber in the tube even after wrapping the helix and the equally good agreement of the measured values with the theory for different pitch lengths it can be concluded that the tubing reduced this effect sufficiently.

To get the final error bars the uncertainty in the readings had to be taken into account as well. As mentioned before, these were estimated to be $\pm 3°$ or ± 0.05 rad. Adding the absolute uncertainties gives the error bars shown in fig.4.1.c. Since the bend induced birefringence was calculated for A=0, only the error bars for the corresponding data points were drawn in the graph.

It can be seen that it is possible to draw the expected straight line through the data points including uncertainties.

Conclusion:

The theory of the quantitative explanation of Berry's topological phase has been verified. The errors and uncertainties involved were found to be reasonably small. This demonstrates good agreement of theoretical and experimental values for different solid angles on the Poincaré sphere in momentum space given by uniform and harmonic deformed helically wound fiber.

5. Magnetooptic Sensing Utilizing the Geometric Rotation

5.1 Measurements of the Fiber Characteristics

The objective of this chapter is to determine the following fiber characteristics experimentally:

a) Elastooptic coefficient

b) Intrinsic birefringence

These parameters are important for the theoretical calculation of the evolution of polarized light as described in chapters 2 and 3. In particular many fiber optic applications utilizing the state of polarization depend strongly upon the characteristics mentioned above. In this study the measurements are needed to construct a magneto-optic currents sensor as it is performed in chapter 5.2.

The single mode fibers investigated were donated by Corning Glass Works and had the following specifications:

1. Hepcor-850 Fiber # unknown

   coating: 500μm cladding: 125μm core: 4-5μm

   numerical aperture NA= 0.14 (specifications)

   V-number V= 2.33 at 850nm (calculated)

   optimum wavelength 850nm, stepped index profile

2. Hepcor-633 Fiber # 6663.02 Sample # 0318

coating: 200μm cladding: 80μm core: 3-4μm

numerical aperture NA= 0.12± 0.02 (measured)

V-number V= 2.08± 0.3 at 633nm (calculated)

optimum wavelength 633nm, stepped index profile

The numerical aperture was determined by measuring the spot size of the emerging beam as a function of the distance from the fiber end. Using equations (1.1.3) and (1.2.5) the numerical aperture and the V-number can be found.

The experimental setup to measure the fiber characteristics mentioned above is shown in Fig.5.1.a. A He-Ne laser with linear polarized output at 633nm and a quarter wave plate were used to produce linear and circular polarized light for measurements a) and b), respectively. The light was launched into the fiber with a microrcopic lens, an x-y-z positioner was used to hold the fiber. The other end went through the center of a rotational stage where it was held by paraffin wax. Therefore variable twist rates could be introduced to the fiber. An analyzer and a power meter as the intensity detector were used to determine the SOP of the emerging light which was measured as a function of the twist rate.

The same precautions were taken for the cleaving and mounting of the fiber as in the experiment in chapter 4 to get a good coupling and to avoid stress on the fiber. A coupling efficiency of 50% to 70% could be achieved which was sufficient to get stable intensity measurements behind the analyzer.

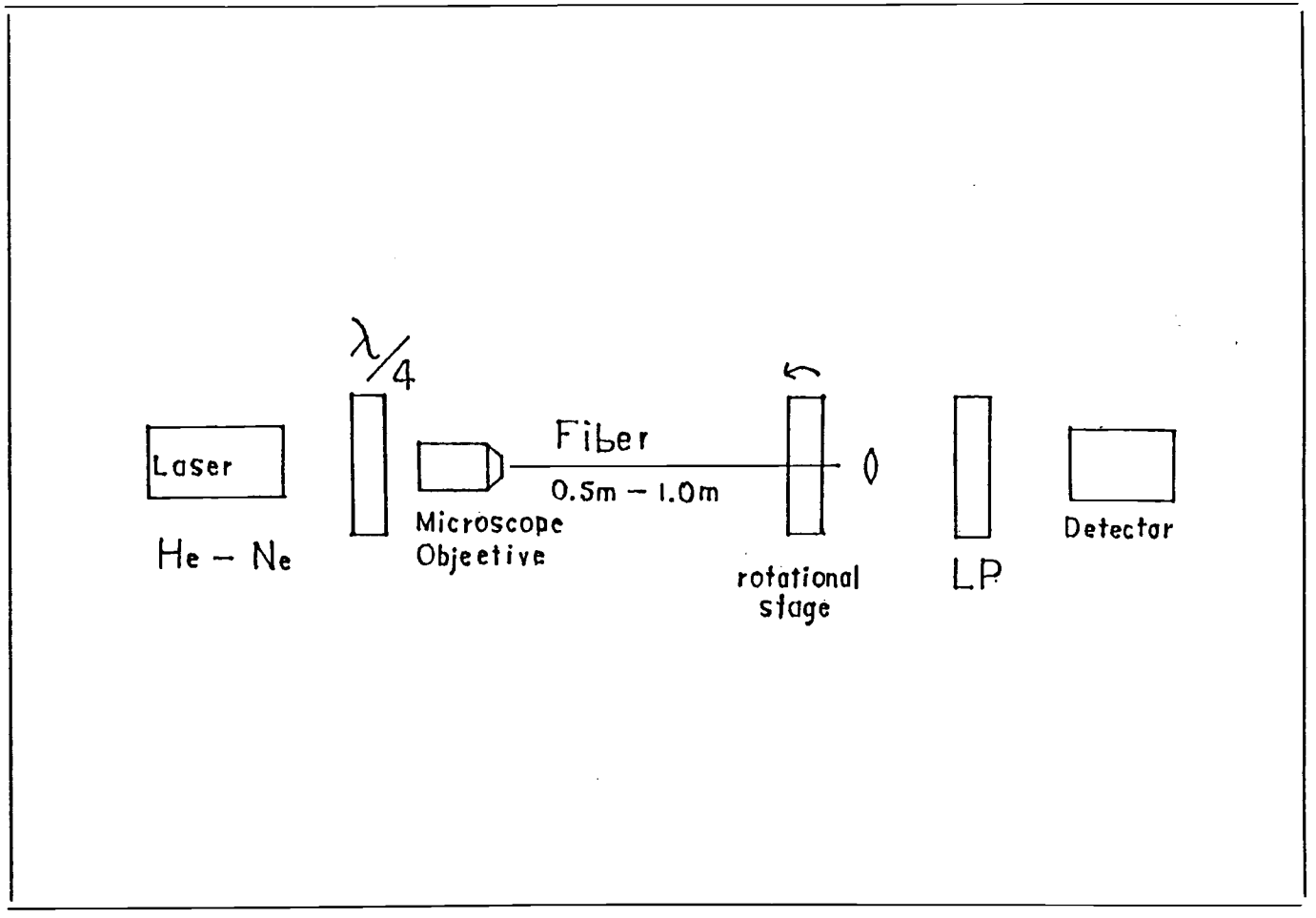

Fig.5.1.a The experimental setup

a) Elastooptic coefficient

The elastooptic coefficient g determines the twist induced birefringence in equation (2.3.13). It can be found by measuring the rotation ϕ of the linear input polarization as a function of the twist rate which gives the twist induced birefringence

$$\alpha = 2 \cdot \phi = g \cdot \chi \qquad (5.1.1)$$

and the g-factor can be deduced. Figures 5.1.b and 5.1.c show the plots of the rotation ϕ of the SOP versus twist rate χ for fibers 1) and 2), respectively. The uncertainty in the maximum intensity position of the analyzer was estimated to be ±10° which was drawn as error bars in the graphics. The results are

1) Hepcor-850 $g = 0.18 \pm 0.02$

2) Hepcor-633 $g = 0.16 \pm 0.01$

The theoretically calculated value for g is given with $g \simeq 0.13$-0.16. The discrepancy may be the result of the calculations being based upon the doping dependent strain-optic coefficients of the fiber. Other measurements of the elastooptic coefficient agree with a slightly higher value.

The knowledge of the g-factors is necessary to find the intrinsic birefringence in part b).

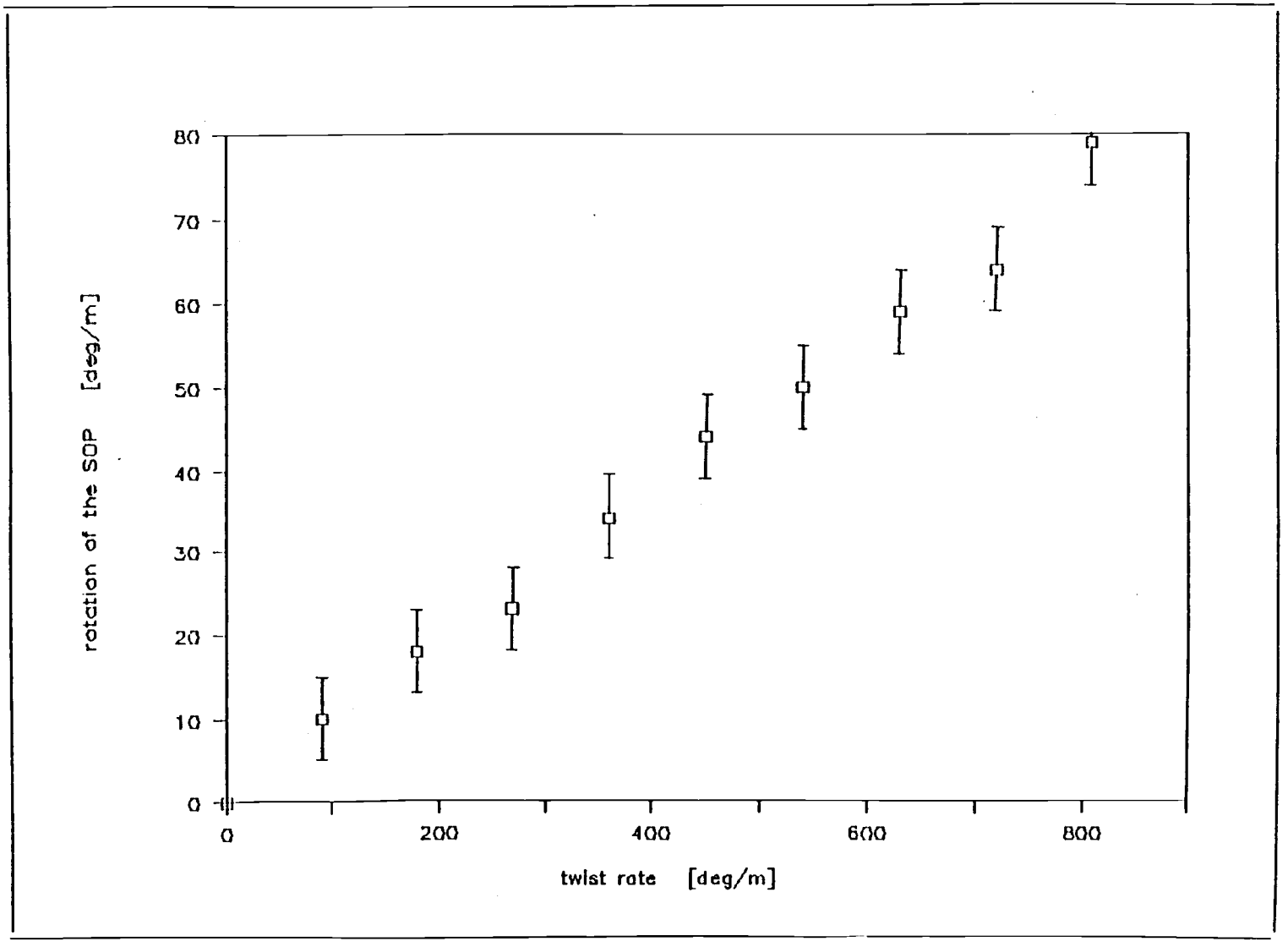

Fig. 5.1.b Rotation of the SOP versus twist rate for fiber 1)

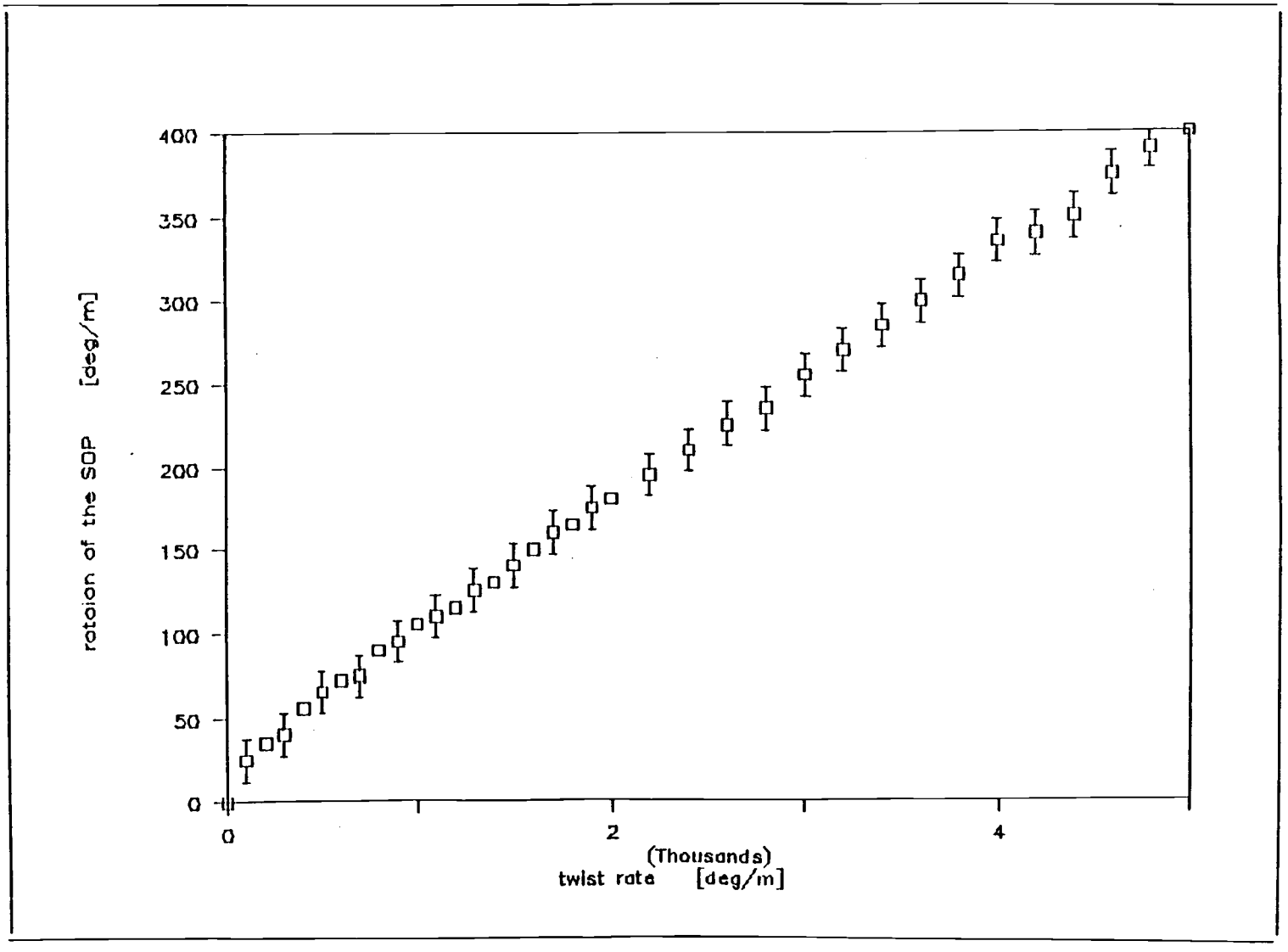

Fig. 5.1.c Rotation of the SOP versus twist rate for fiber 2)

b) The intrinsic birefringence

Many methods have been developed to measure the intrinsic birefringence:

(i) direct visualisation of the beat length by Rayleigh scattering. Applicable for 1mm< L_b < 10cm.[18]

(ii) measurement of the SOP with linearly polarized input for various lengths of the straight fiber in the range 1cm < L_b < 10m.

(iii) electro- and magnetooptical modulation of the SOP on a small test section of the fiber (0.1-1cm) yielding the local intrinsic birefringence.

(iv) the POTDR method which allows measurements of 1m < L_b < 100m.

The method used in this study was proposed by M. Monerie and P. Lamouler in 1981.[24] It measures the ellipticity of the SOP of the outcoming light as a function of the twist rate introduced to the fiber. Using the system matrix (2.3.11) derived in chapter 2 for the coupling of homogeneous linear and circular birefringence the intrinsic birefringence can be deduced by comparison of theory and experiment if the elastooptic coefficient is known. The advantages to the other methods mentioned above are

- the simplicity of the experimental setup
- the method is nondestructive
- the same experimental setup can be used to measure the elastooptic coefficient as performed in part a)

In addition, as a result of this study, this method seems to provide information about the uniformity of the fiber.

Theory:

A homogeneously twisted fiber with homogeneous intrinsic birefringence can be described by the system matrix (2.3.11). The eigenmodes of this system are straight elliptical and they exhibit a phase difference Δl as the light propagates through the fiber which is such that:[24,12]

$$\cos(\Delta l) = \frac{1 + \eta^2 \cos(2\psi)}{1+\eta^2} \qquad (5.1.2a)$$

where

$$\eta = \frac{\beta z}{|\chi| \cdot (2-g)} \qquad (5.1.2d)$$

$$\psi = \frac{1}{2} \cdot |\chi^2 \cdot (2-g)^2 + (\beta z)^2|^{\frac{1}{2}} \qquad (5.1.2c)$$

with $\beta = |k_x - k_y|$ for the straight, untwisted fiber. The SOP is characterized by the polarization ellipticity ϵ, defined as

$$\epsilon = \frac{(I_M - I_m)}{(I_M + I_m)} \qquad (5.1.3)$$

with the uncertainty

$$\delta\epsilon = 2\epsilon \cdot \delta I \cdot \frac{(I_M^2 + I_m^2)^{\frac{1}{2}}}{(I_M^2 - I_m^2)} \qquad (5.1.4)$$

where I_M, I_m are the maximum and minimum intensities passing through the analyser whose direction is varied and δI is the estimated uncertainty in the intensity measurement. If the input SOP is circular

(ϵ=0), then the ellipticity of the SOP at the output is related to the phase difference Δl by $\epsilon = |\sin(\Delta l)|$ and with equations (5.1.2a-c) we obtain:

$$\epsilon = \frac{2\eta}{1+\eta^2} \cdot (1 + \eta^2 \cdot \cos^2(\psi))^{\frac{1}{2}} \cdot |\sin(\psi)| \qquad (5.1.5)$$

Measuring the ellipticity as a function of the twist rate, the intrinsic birefringence can be deduced by comparison of theory and experiment if the elastooptic coefficient is known.

Fig.5.1.d shows the function (5.1.5) for two different values of β. It can be seen, that the major changes in the behaviour of the function happen around the detwist point, whereas the maxima and minima positions on the x-axis hardly depend upon β. Therefore the method used to deduce β was to vary it until the least standard deviation between theory and experiment was achieved were there was more weight on the data around the detwist point.

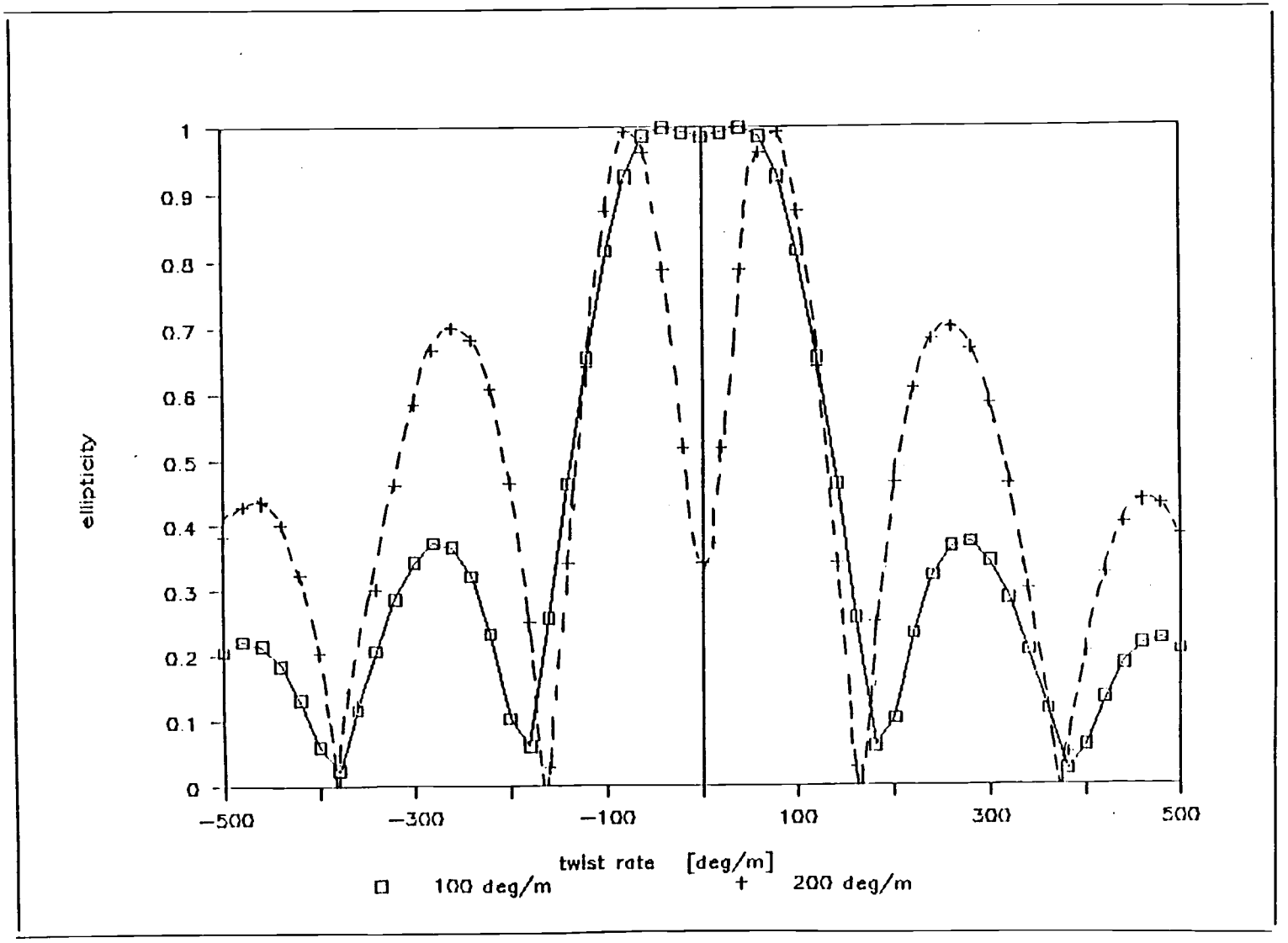

Fig. 5.1.d Theoretical calculation of the output ellipticity

Data Analysis:

1. Hepcor-850

Fig.5.1.e shows the experimental and theoretically fitted curve of the ellipticity versus twist. The offset in the twist can be determined by the required symmetry of the curve. A better accuracy can be achieved, however, by the computational variation of twist offset and intrinsic birefringence to find the minimum standard deviation $\sigma(\epsilon)$ in the ellipticity. For this fiber the minimum in $\sigma(\epsilon)$ was found to be 0.047 with an intrinsic birefringence of β=105deg/m and a twist offset of 80deg/m. The result for $\sigma(\epsilon)$ agrees with the error bars calculated using equation (5.1.4) and Fig.5.1.e shows, that the theoretical curve using the parameters above fits pretty well into the error bars. To exclude ambiguities in β, the standard deviation was calculated as a function of β for a twist offset of 80deg/m which is shown in Fig.5.1.f. It is seen, that there is no other local minimum, and as it has been verified that this also holds for a larger range of β. This also has been used to find an estimation of the uncertainty in β. Table 5.1.I shows a summary of the results.

Table 5.1.I

Specifications of fiber type 1.Hepcor-850

g-factor	intrinsic birefringence β	intrinsic twist
0.18 ± 0.02	105deg/m ± 20deg/m	80deg/m ± 20deg/m

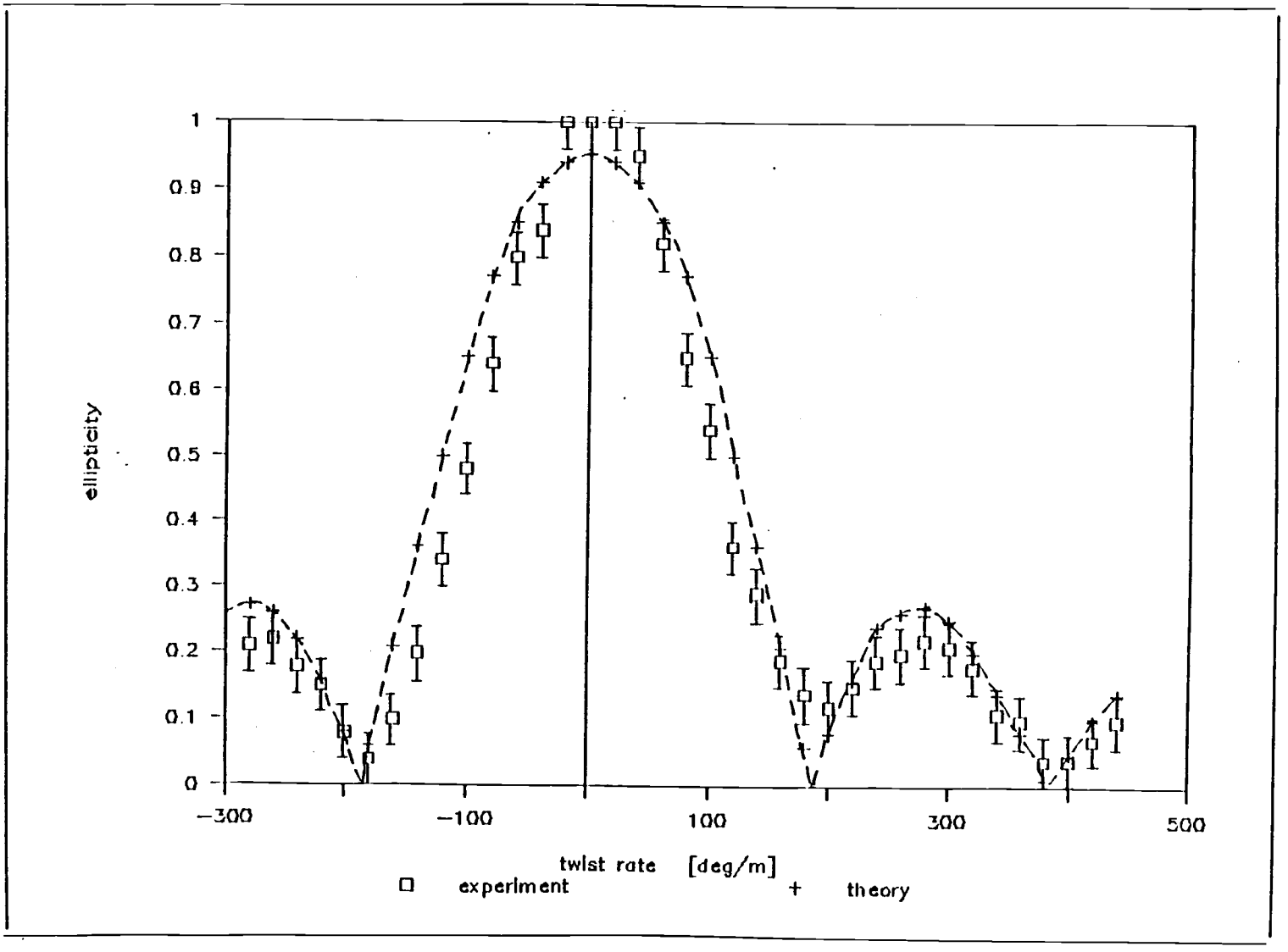

Fig. 5.1.e Experimental and fitted curve for fiber type 1)

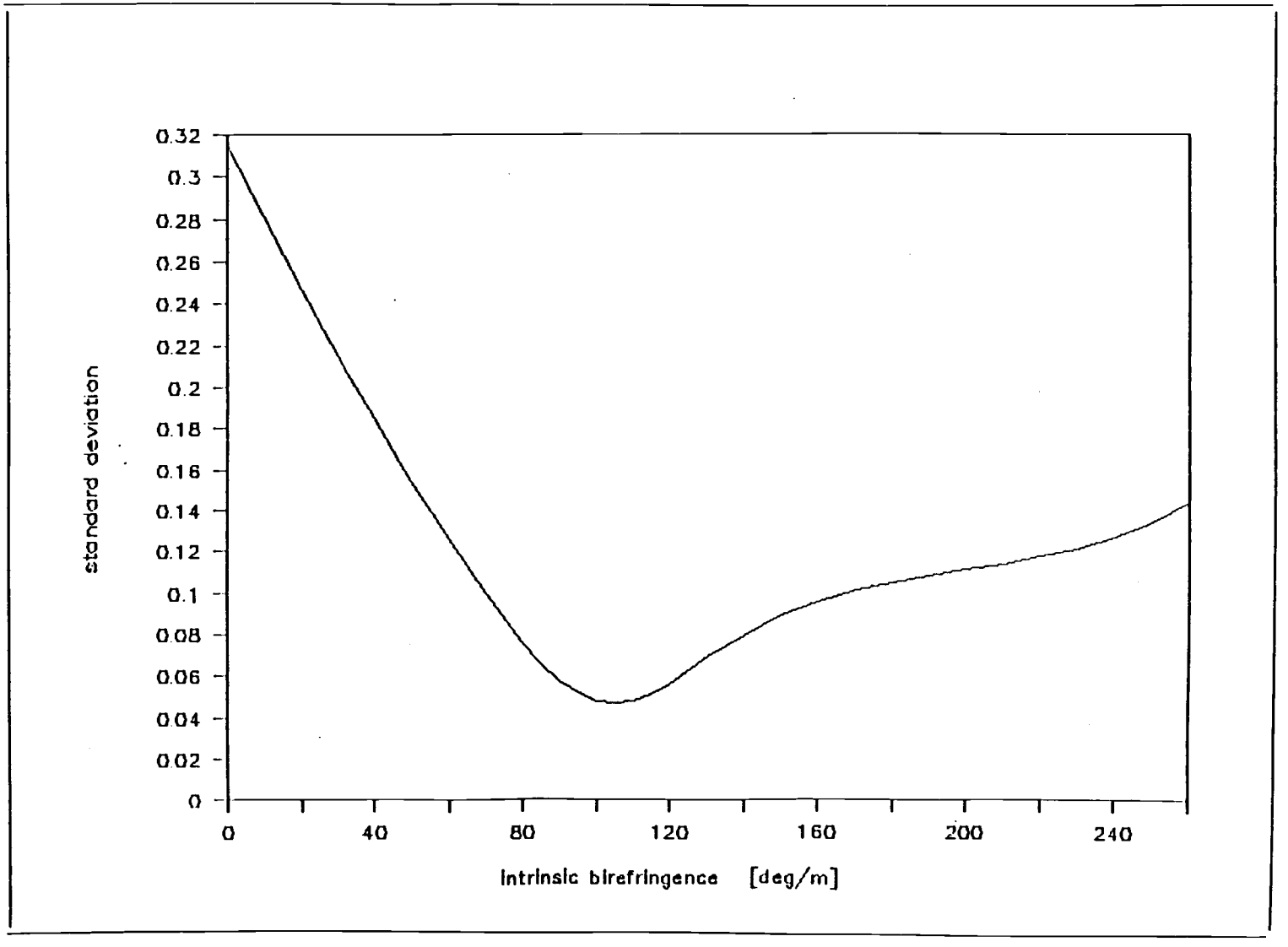

Fig. 5.1.f The standard deviation versus birefringence for fiber 1)

2. Hepcor-633

In this case the results didn't come out as well as those for fiber 1. In fact, it turned out to be impossible to find a set of parameters such that the theoretical curve fits all the data. However, a fitting curve could be found for a twist range either from 0° to 150° or from 150° to 380°. As shown in Fig.5.1.d, the most significant changes in the curve happen around the origin which suggests taking those data into consideration. Unfortunately, this still leaves some ambiguities in the result. Fig.5.1.g shows the standard deviation as a function of β for a twist offset of 70deg/m, which could be determined out of symmetry. There are several local minima which are all possible solutions. The first minimum at β=80deg/m, however, can be excluded since the overall behavior of the curve is different from the experiment as it is the case for all the minima above β=360deg/m. The other two solutions at β=240deg/m and β=330deg/m seem to be almost equally likely. For clarity, Fig.5.1.h shows the experimental and theoretically fitted curve only for β=240deg/m, but as a result both solutions may be considered as being possible. Table 5.1.II summarizes the results.

Table 5.1.II

Specifications of fiber type 2.Hepcor-633

g-factor	intrinsic birefringence	intrinsic twist
0.16 ± 0.01	240/330deg/m ± 30deg/m	70deg/m ± 20deg/m

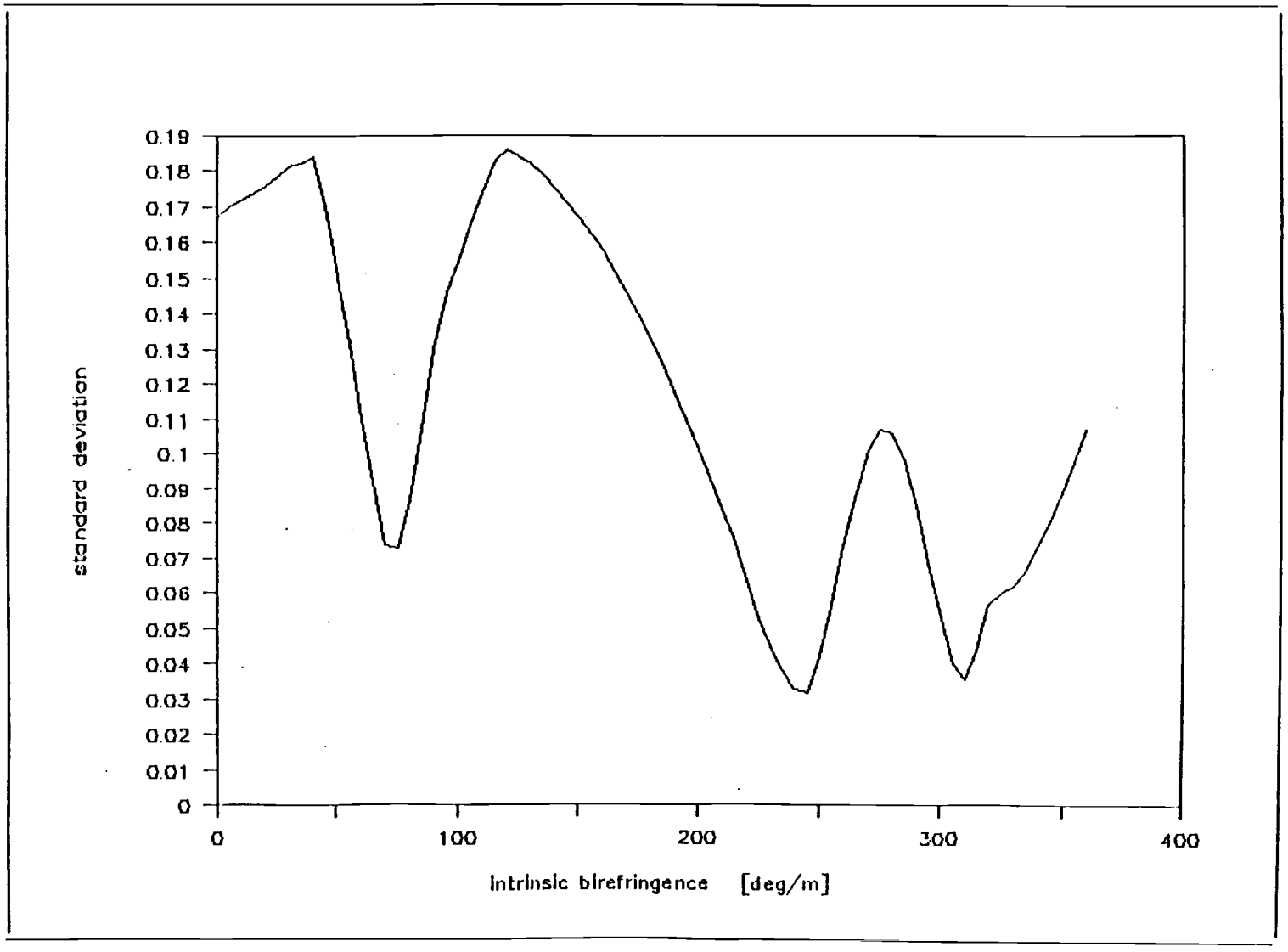

Fig. 5.1.g The standard deviation versus birefringence for fiber 2)

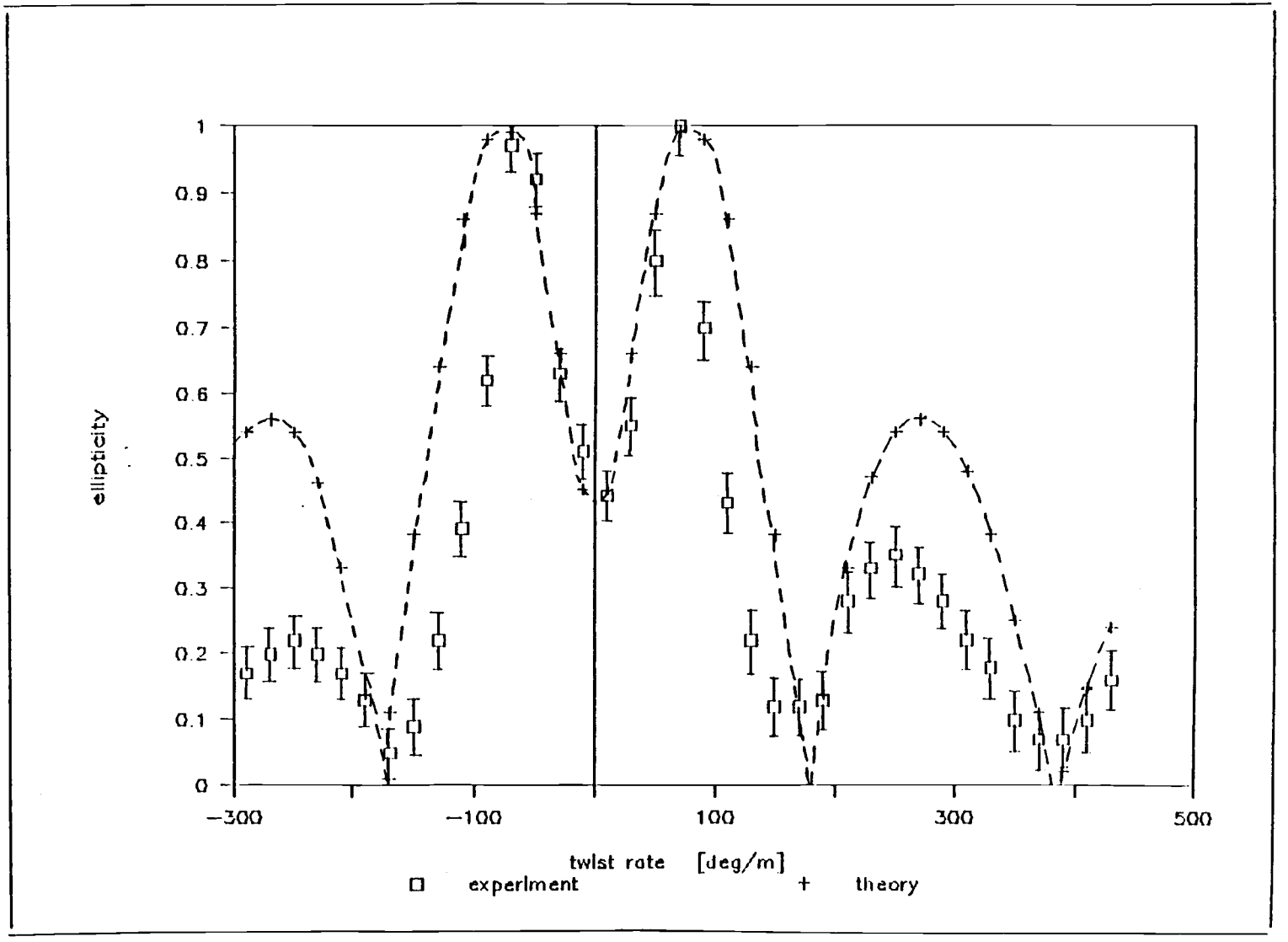

Fig. 5.1.h Experimental and fitted curve for fiber 2)

Conclusion:

The theory described the evolution of polarization only for fiber type 1. Reasons for the disagreement in case of fiber 2 may be

i) uncertainty in the g-factor which is a parameter in the theory

ii) inhomogenities in the intrinsic birefringence or the induced twist.

i) the g-factor

The g-factor has been determined in part a) of this chapter. It has been verified, that varying the g-factor within the uncertainty range does not change the results of part b) significantly.

ii) inhomogenities in the intrinsic birefringence or the induced twist

This seems to be the only explanation for the discrepancy between theory and experiment. The theory is derived from the system matrix (2.3.11) for the coupling of homogeneous linear and circular birefringence. For inhomogeneous coupling the birefringence becomes z-dependent and the evolution of polarization cannot be calculated anymore as described in chapter 2. Thus the disagreement in the case of fiber type 2.Hepcor-633 leads to the conclusion, that either the intrinsic birefringence or the induced twist are inhomogeneous. This is an important result since for many applications it is necessary to apply the system matrix (2.3.11) in order to evaluate the evolution of polarization.

5.2 The Magnetooptic Current Sensor Design

Many efforts have been made in the past 8 years to use the Faraday effect in an optical fiber for magnetooptic sensing.[25-29] The advantages over conventional induction coil sensors are

(i) the fiber is a dielectric component which allows high voltage applications and measurements without interference with the magnetic field.

(ii) The response time is in the order of 0.1ns, which is mainly determined by the length of the fiber and the speed of light.

(iii) The fiber acts as transmission line and sensing element.

(iv) DC and high bandwidth AC current measurements are possible.

Using the Verdet constant for silica the minimum detectable magnetic field ranges approximately from 1 to 10 Gauss, depending upon the detection system. For the measurement of a current passing through a fiber coil this means that the sensitivity range is rather high, usually above 1000A. With these properties the magnetooptic sensing has been used already for high and short pulse current measurements in a high voltage environment.[29] However, there are other problems introduced using optical fibers. As described in chapter 3.1, there is also intrinsic and bend induced linear birefringence in addition to the Faraday induced circular birefringence. Due to the presence of linear birefringence the circular SOP's aren't eigenstates anymore. This suppresses the rotation of the SOP which can be expressed in smaller effective Verdet constant and equation (3.1.3) becomes [28]

$$\alpha = 2V_{eff} \cdot \int \vec{H} \cdot d\vec{l} \qquad (5.2.1).$$

For the application of sensoring currents with fiber optics, the bend induced birefringnce usually becomes large by wrapping the fiber as a coil around the current. On the other hand, since the magnetic field due to a current is rather weak, a high Verdet constant is desired . This can be achieved by introducing a high bias circular birefringence $\alpha >> \beta$ which makes the linear birefringence negligible and the system matrix reduces to

$$M = \begin{bmatrix} \cos(\Gamma z) & \sin(\Gamma z) \\ -\sin(\Gamma z) & \cos(\Gamma z) \end{bmatrix} \qquad (5.2.2)$$

where $\Gamma = 1/2 \cdot \alpha$. Matrix (5.2.2) is a simple rotator and the effective Verdet constant is equal to the one for fused silica mentioned above.[27] In the past the bias cicular birefringence has been achieved by twisting the fiber with rather high twist rates in the order of 10 to 20 turns/m to overcome the linear birefringence.[27] However, the problem is to keep the fiber from detwisting which requires an extra jacket to lock the twist. In this study, the possibility of introducing the bias circular birefringence utilizing the geometric rotation is investigated. The advantages would be that no twist is necessary. The theory for the geometric rotation is given in chapter 3.2. It was shown, that the path of the fiber has to leave its plane of curvature to introduce a circular birefringence. The uniform helix is the simplest geometry where this is fulfilled. As a current sensor,

however, the geometry of a toroidal helix shown in Fig.5.2.a is much more appropriate since it is of a smaller size while the geometric rotation can still be calculated. The equations are derived in chapter 3.3. The geometric rotation (3.3.13) has been evaluated numerically using the Simpson rule and normalized with (3.3.14).

In order to predict the applicability of this sensor design, the geometric rotation (3.3.13) has been compared with the bend induced birefringence given by (3.1.1) and the intrinsic birefringence determined experimentally in chapter 5.1. The calculations were done for various values of the toroid thickness r while the inner radius of the toroid, R-r, was kept constant. Fig.5.2.b shows the geometric rotation as a function of the toroid thickness for two different values of the inner radius. It is seen, that the behaviour is qualitatively similar where there is a maximum at approximately $r=2.4\cdot(R-r)$ or $r/R=0.7$. This result was found to be a general characteristics in the range of interest for the inner radius and can therefore be used to find the toroid dimensions for the maximum geometric rotation. Evaluating the curvature for this geometry using (3.2.3) yields that it varies within one cycle. Thus there are points of maximum and minimum curvature which have been determined.

Table 5.2.I presents the results of interest for the inner toroid radius R-r between 0.02m and 0.2m where $r/R=0.7$.

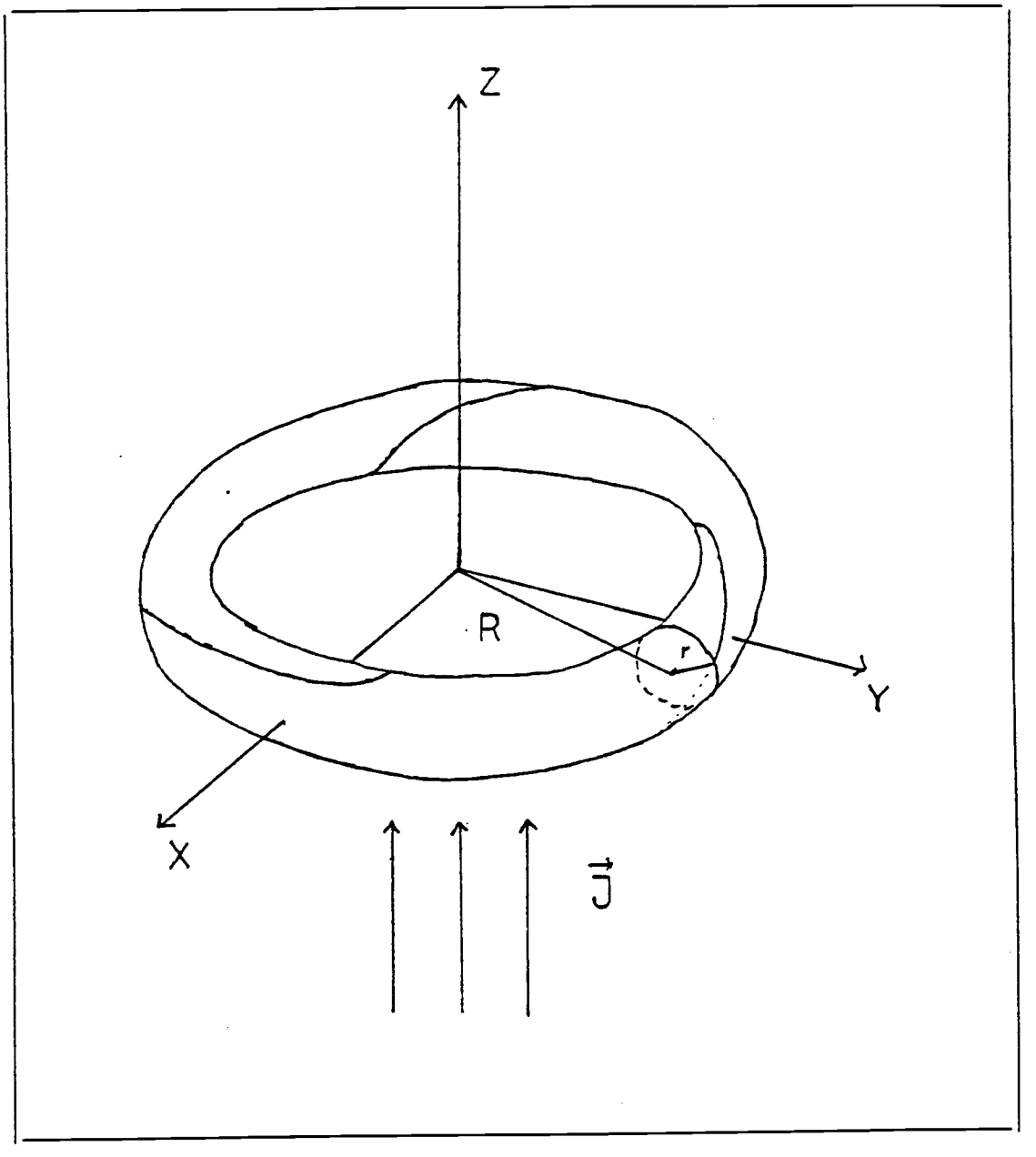

Fig.5.2.a Geometry of the toroidal fiber optic current sensor

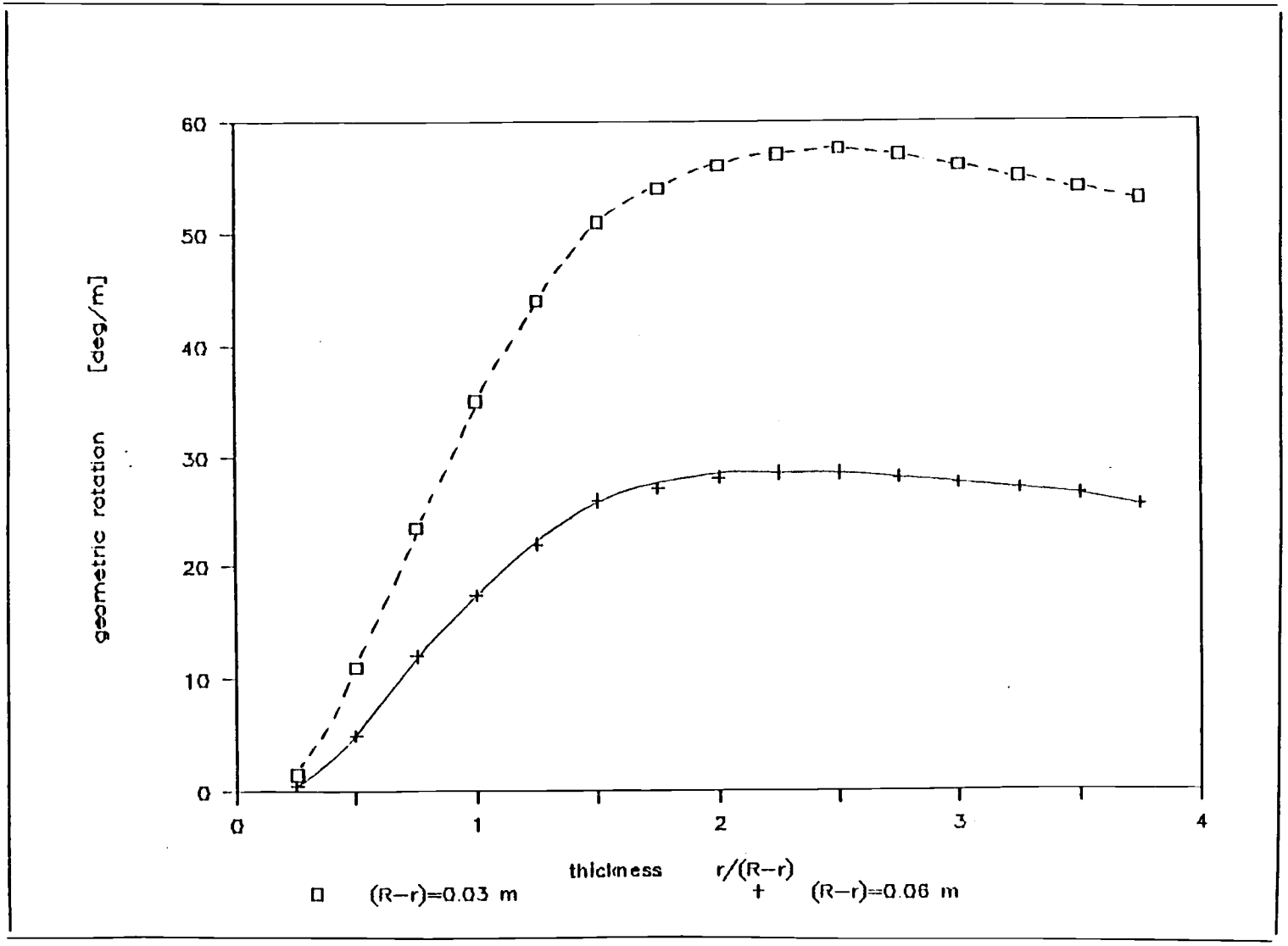

Fig. 5.2.b Geometric rotation versus toroid thickness

Table 5.2.I

The maximum geometric rotation in deg/m for one turn on a toroid compared to the maximum and minimum bend induced birefringence

Fiber type 1.Hepcor-850:
intrinsic birefringence: β= 105 ± 20deg/m
cladding diameter: 125μm

inner radius R-r in [m]	geometric rotation [deg/m]	bend induced birefringence maximum [deg/m]	minimum
0.02	86.0	140.6	32.3
0.04	43.0	35.2	8.1
0.06	28.7	15.7	3.6
0.08	21.5	8.8	2.1
0.10	17.2	5.7	1.3
0.12	14.3	4.0	0.9
0.14	12.3	2.9	0.7
0.16	10.7	2.2	0.6
0.18	9.6	1.8	0.4

Fiber type 2.Hepcor-633:
intrinsic birefringence: β= 240/330 ± 30deg/m
cladding diameter: 80μm

inner radius R-r in [m]	geometric rotation [deg/m]	bend induced birefringence maximum [deg/m]	minimum
0.02	86.0	57.6	13.3
0.04	43.0	14.4	5.9
0.06	28.7	6.4	1.5
0.08	21.5	3.6	0.9
0.10	17.2	2.4	0.6
0.12	14.3	1.6	0.4
0.14	12.3	1.2	0.3
0.16	10.7	0.9	0.3
0.18	9.6	0.8	0.2

Due to the pitch angle of the helix, the component of the magnetic field parallel to the fiber B_{eff} is approximately

$$B_{eff} \simeq B \cdot \frac{R}{N \cdot (R^2+r^2)^{\frac{1}{2}}} \qquad (5.2.3)$$

where N is the number of turns on the toroid. Using $r=0.7 \cdot R$ this comes out to be

$$B_{eff} \simeq 0.82 \cdot \frac{B}{N} \qquad (5.2.4).$$

Discussion of the results:

In order to obtain a high Verdet constant for weak magnetic fields, the sum of intrinsic and bend induced birefringence has to be much smaller than the bias circular birefringence. Using the results in table 5.2.I, this is not the case for the geometry and fiber types suggested. However, using single-mode fiber with very low intrinsic birefringence, which may be available soon, the method becomes very interesting. Also, as the cladding diameter of the core can be made smaller, the bend induced birefringence will be reduced and may be negligible compared to the geometric rotation. The desired specifications for the fiber therefore would be $\beta \simeq$ 10deg/m and a 40μm cladding diameter.

Another possibility finally is to leave the path of a uniform helix and find the path of the smallest curvature on the toroid. This, however, would make the calculation of the geometric rotation impossible.

References

1. L. Jeunhomme, 'Single Mode Fiber Optics: Principles and Applications', (Marcel Dekker, New York, 1988)

2. A. Yariv, 'Optical Electronics', (Holt, Rinehart and Winston, New York, 1985)

3. D. Gloge, Appl. Opt., 10, 2252 (1971)

4. E. Hecht, 'Optics', (Addison-Wesley, Mass., 1987)

5. M. Born, 'Principles of Optics', (Pergamon Press, New York, 1959)

6. J.D. Jackson, 'Classical Electrodynamics',Wiley & Sons, New York, 1975

7. R.C. Jones, J. Opt. Soc. Am., 31, 488 (1941)

8. R.C. Jones, J. Opt. Soc. Am., 36, 486 (1942)

9. R.C. Jones, J. Opt. Soc. Am., 38, 671 (1948)

10. Americam Association of Physics Teachers, 'Polarized Light', (AIP, New York, 1954)

11. S.C. Rashleigh, J. Lightwave Technol., LT-1, 312 (1983)

12. M. Monerie, L. Jeunhomme, Opt. & Quantum Electron., 12, 449 (1980)

13. A. Simon and R. Ulrich, Appl. Phys. Lett., 31, 517 (1977)

14. A. Simon and R. Ulrich, Appl. Opt., 18, 2241 (1979)

15. A.M. Smith, Appl. Opt., 17, 52 (1978)

16. A.M. Smith, Appl. Opt., 19, 2606 (1980)

17. R. Ulrich, S.C. Rashleigh, W. Eickhoff, Opt. Lett., 5, 273 (1980)

18. I.P. Kaminow, J. Quantum Electron., QE-17, 15 (1981)

19. J.N. Ross, Opt. & Quantum Electron., 16, 455 (1984)

20. A. Tomita, R.Y. Chiao, Phys. Rev. Lett., 57, 937 (1986)

21. M.V. Berry, Letters to Nature, 326, 277 (1987)

22. F.D.M. Haldane, Opt. Lett., 11, 730 (1986)

23. M. Schwartz, S. Green, W. Rutledge, '<u>Vector Analysis with Applications to Geometry and Physics</u>', (Harper & Row, New York, 1980)

24. M. Monerie, P. Lamouler, Opt. & Quantum Electron., <u>14</u>, 41 (1981)

25. S.C. Rashleigh, R. Ulrich, Appl. Phys. Lett., <u>34</u>, 768 (1979)

26. A. Papp, H. Harms, Appl. Opt., <u>19</u>, 3729 (1980)

27. G. Chandler, F. Jahoda, Rev. Sci. Instrum., <u>56</u>, 852 (1985)

28. F. Buchholtz, K. Koo, A. Kersey, A. Dandridge, SPIE, <u>718</u>, 56 (1986)

29. H.S. Lassing, A. Oomens, R. Woltjer, Rev. Sci. Instrum., <u>57</u>, 851 (1986)

30. J. Noda, K. Okamoto, Y. Sasaki, J. Lightwave Tech., <u>LT-4</u>, 1071 (1986)